

The *Chandra* High-Energy Transmission Grating: Design, Fabrication, Ground Calibration, and 5 Years in Flight

CLAUDE R. CANIZARES, JOHN E. DAVIS, DANIEL DEWEY, KATHRYN A. FLANAGAN, EUGENE B. GALTON,
DAVID P. HUENEMOERDER, KAZUNORI ISHIBASHI, THOMAS H. MARKERT, HERMAN L. MARSHALL, MICHAEL MCGUIRK,
MARK L. SCHATTEBURG, NORBERT S. SCHULZ, HENRY I. SMITH, AND MICHAEL WISE

MIT Kavli Institute, Massachusetts Institute of Technology, Cambridge, MA 02139; crc@space.mit.edu

Received 2004 August 28; accepted 2005 June 21; published 2005 September 20

ABSTRACT. Details of the design, fabrication, and ground and flight calibration of the High Energy Transmission Grating (HETG) on the *Chandra X-Ray Observatory* are presented after 5 years of flight experience. Specifics include the theory of phased transmission gratings as applied to the HETG, the Rowland design of the spectrometer, details of the grating fabrication techniques, and the results of ground testing and calibration of the HETG. For nearly 6 years the HETG has operated essentially as designed, although it has presented some subtle flight calibration effects.

1. INTRODUCTION

The *Chandra X-Ray Observatory* (Weisskopf et al. 2000), formerly the *Advanced X-Ray Astrophysics Facility (AXAF)*, was launched on 1999 July 23, and for 5 years has been realizing its promise to open new domains in high-resolution X-ray imaging and spectroscopy of celestial sources (Weisskopf et al. 2004, 2002). The High Energy Transmission Grating (HETG; Canizares et al. 2000) is one of two objective transmission gratings on *Chandra*; the Low Energy Transmission Grating (LETG; Brinkman et al. 2000) is of a similar design but is optimized for energies less than 1 keV. When the HETG is used with the *Chandra* mirror and a focal plane imager, the resulting High Energy Transmission Grating Spectrometer (HETGS) provides spectral resolving powers of up to 1000 over the range 0.4–8 keV (1.5–30 Å) for point and moderately extended sources. Through the year 2004, the HETGS was used in 422 observations covering the full range of astrophysical sources and totaling 20 Ms, or 17% of *Chandra* observing time. Up-to-date information on *Chandra* and the HETG is available from the *Chandra X-ray Center (CXC 2004)*. This paper summarizes the design, fabrication, and ground and flight calibration of the HETG.

The High Energy Transmission Grating (Canizares et al. 1985, 1987; Markert 1990; Schattenburg et al. 1991; Markert et al. 1994) is a passive array of 336 diffraction-grating facets, each about 2.5 cm². Each facet is a periodic nanostructure consisting of finely spaced parallel gold bars supported on a thin plastic membrane. The facets are mounted on a precision HETG element support structure (HESS), which in turn is mounted on a hinged yoke just behind the high-resolution mirror assembly (HRMA; van Speybroeck et al. 1997). A telemetry command to *Chandra* activates a motor drive that inserts the

HETG into the optical path just behind the HRMA, approximately 8.6 m from the focal plane, shown schematically in Figure 1. The lower portion of this figure shows a schematic of the Advanced CCD Imaging Spectrometer (Garmire 1999) spectroscopy detector (ACIS-S), with the HETG's shallow X dispersion pattern indicated. This pattern arises from the use of two types of grating facets in the HETG, with dispersion axes offset by 10° so that the corresponding spectra are spatially distinct on the detector.

The choice (and complexity) of using two types of grating facets resulted from our desire to achieve optimum performance in both diffraction efficiency and spectral resolution over the factor of 20 energy range from 0.4 to 8 keV. These facets are the heart of the HETG and are schematically shown in Figure 2, with their properties given in Table 1. One type, the medium energy grating (MEG), has spatial period, bar thickness, and support membrane thickness that is optimized for the lower portion of the energy range. These MEG facets are mounted on the two outer rings of the HESS so that they intercept rays from the outer two mirror shells of the HRMA, which account for ~65% of the total HRMA effective area below 2 keV. The second facet type, the high-energy grating (HEG), has finer period for higher dispersion, and thicker bars to perform better at higher energies. The HEG array intercepts rays from the two inner HRMA shells, which have most of the area above ~5 keV.

When the HRMA's converging X-rays pass through the transmission grating assembly, they are diffracted in one dimension by an angle β given by the grating equation at normal incidence

$$\sin \beta = m\lambda/p, \quad (1)$$

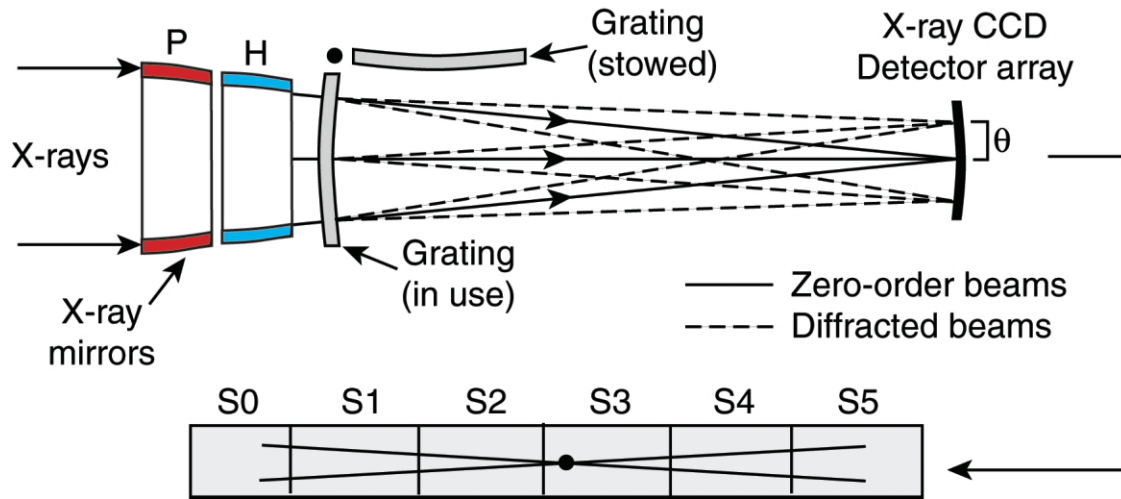


FIG. 1.—Schematic of the HETGS on *Chandra*. The HETGS is formed by the combined operation of the mirror system (HRMA), the inserted HETG, and the ACIS-S detector.

where m is the integer order number, λ is the photon wavelength,¹ p is the spatial period of the grating lines, and β is the dispersion angle. A “normal” undispersed image is formed by the zeroth-order events ($m = 0$), while the higher orders form overlapping dispersed spectra that stretch on either side of the zeroth-order image. By design, the first orders ($m = \pm 1$) dominate. Higher orders are also present; however, the ACIS itself has moderate energy resolution, sufficient to allow the separation of the overlapping diffracted orders.

As with other spectrometers, the overall performance of the HETGS can be characterized by the combination of the effective area encoded in an auxiliary response function (ARF; Davis 2001a) and a line response function (LRF) encoded as a response matrix function (RMF). For this grating system, the LRF describes the spatial distribution of monochromatic X-rays along the dispersion direction; a simple measure of the LRF is the FWHM ($\Delta\lambda_{\text{FWHM}}$), expressed in dimensionless form as the resolving power, $\lambda/\Delta\lambda_{\text{FWHM}} \equiv E/\Delta E_{\text{FWHM}}$. With the HRMA’s high angular resolution (better than $1''$), the HETG’s high dispersion (as high as $100'' \text{ \AA}^{-1}$), and the small, stable pixel size ($24 \mu\text{m}$, or $\sim 0.5''$) of ACIS-S, the HETGS achieves spectral resolving powers up to $E/\Delta E \approx 1000$.

The following sections present details of the key ingredients and papers related to the design of the HETGS, the fabrication and testing of the individual HETG grating facets, and the

results of full-up ground calibration of the flight HETG. The final section (§ 5) demonstrates the HETGS flight performance and discusses the calibration status of the instrument after 5 years of flight operation.

2. HETG DESIGN

2.1. Theory of Phased Transmission Gratings

Obtaining high throughput requires that X-rays are dispersed into the $m = \pm 1$ orders with high diffraction efficiency. This is largely determined by the microproperties of the MEG and HEG grating bars and support membranes. Both the MEG and HEG facets are designed to operate as “phased” transmission gratings to achieve enhanced diffraction efficiency over a significant portion of the energy range for which they are optimized (Schnopper et al. 1977). A conventional transmission

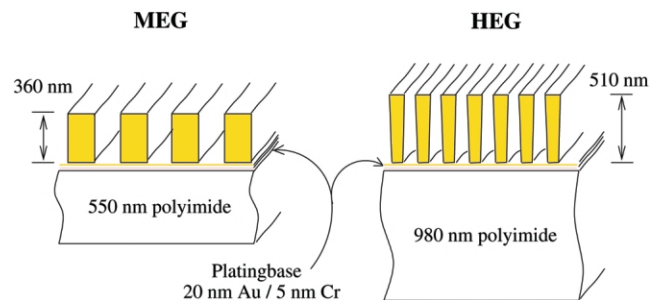


FIG. 2.—HETG grating cross-sections. The soap-bubble-thin grating membranes of the HETG facets consist of a supporting polyimide layer, a thin Cr/Au plating base layer, and the actual Au grating bars. The figures are to scale, and dimensions are approximate average values. Note the high aspect ratio for the HEG grating bars.

¹ Wavelength bins are “natural” for a dispersive spectrometer (e.g., the dispersion and spectral resolution $[\Delta\lambda]$ are nearly constant with λ), and wavelength is commonly used in the high-resolution X-ray spectroscopy community. However, since photon energy has been commonly used in high-energy X-ray astrophysics (as is appropriate for nondispersive spectrometers like proportional counters and CCDs), we use either energy or wavelength values interchangeably, depending on the context. The values are related through $E \times \lambda = 12.3985 \text{ keV \AA}^{-1}$.

TABLE 1
KEY FABRICATION, GROUND TEST, AND FLIGHT PARAMETERS OF THE HETG

Parameter Name	Value	Comments
Grating Facet Parameters		
Grating bar material	Gold	...
HEG, MEG bar thickness (nm)	510, 360	Approximate average value
HEG, MEG bar width (nm)	120, 208	Approximate average value
HEG, MEG polyimide thickness (nm)	980, 550	Approximate average value
Plating base thicknesses (nm)	20 (Au), 5.0 (Cr)	Approximate average value
HETG Laboratory Parameters		
HESS Rowland diameter (mm)	8633.69	As designed and machined
HEG average period (Å)	2000.81 ± 0.05	LR, NIST referenced
MEG average period (Å)	(4001.41 ± 0.22)	Updated in flight (see below)
Vignetting, shell 1	0.937 ± 0.01	Interfacet vignetting, from calculation
Vignetting, shell 3	0.940 ± 0.01	Interfacet vignetting, from calculation
Vignetting, shell 4	0.931 ± 0.01	Interfacet vignetting, from calculation
Vignetting, shell 6	0.936 ± 0.01	Interfacet vignetting, from calculation
Efficiencies (rev. N0004)	Fig. 17	from X-GEF measurements and synchrotron optical constants
XRCF Measurement Results		
Rowland spacing at XRCF (mm)	8782.8 ± 0.6	Assuming lab periods
HEG angle (deg)	-5.19 ± 0.05	With respect to XRCF axes
MEG angle (deg)	4.74 ± 0.05	With respect to XRCF axes
HEG-MEG opening angle (deg)	9.934 ± 0.008	From beam center data
HEG dp/p (ppm rms)	146 ± 50	Mg K slit scan analysis
MEG dp/p (ppm rms)	235 ± 50	Mg K slit scan analysis
HEG roll variation (arcmin rms)	≈1.8	Two peaks, 3' apart
MEG roll variation (arcmin rms)	≈1.8	≈Gaussian distribution
Misaligned MEGs (arcmin)	3-25	6 MEG roll outliers
HEG contribution to LRF wing ($1/\text{Å} \times \text{Å}^2$)	$\leq 1.3 \times 10^{-4}$	At Mg K, 9.887 Å (see text)
MEG contribution to LRF wing ($1/\text{Å} \times \text{Å}^2$)	$\leq 2.0 \times 10^{-4}$	At Mg K, 9.887 Å (see text)
HEG scatter (%/Å)	≈0.2	At 7 Å; ≤ 1% total
MEG scatter	Not seen	<1/10th of HEG value
Flight Results		
Rowland spacing (mm)	8632.65	As installed; sets wavelength scale
HEG angle (deg)	-5.235 ± 0.01	With respect to ACIS-S3 CHIPX axis
MEG angle (deg)	4.725 ± 0.01	With respect to ACIS-S3 CHIPX axis
HEG average period (Å)	2000.81 ± 0.05	Retains ground calibration value
MEG average period (Å)	4001.95 ± 0.13	Based on Capella-HEG results

grating with *opaque* grating bars achieves a maximum efficiency of 10% in each ± 1 st order for the case of equal bar and gap widths (Born & Wolf 1980, pp. 401–414). In contrast, the grating bars of the MEG and HEG are partially transparent; X-rays passing through the bars are attenuated and also phase shifted, depending on the imaginary and real parts, respectively, of the index of refraction at the given λ . Ideally, the grating material and thickness can be selected to give low attenuation and a phase shift of $\approx \pi$ radians at the desired energy (Schatzenburg 1984). This causes the radiation that passes through the bars to destructively interfere with the radiation that passes through the gaps when in zeroth order (where the relevant path lengths are equal), reducing the amount of undiffracted (zeroth order) radiation and, conversely, enhancing the diffracted-order efficiency. In practice, this optimal phase interference can only be obtained over a narrow wavelength band, as seen in Fig-

ure 3, because of the rapid dependence of the index of refraction on wavelength. Initial designs based on these considerations suggested using gold for the HEGs and silver for the MEGs; in the end, fabrication considerations lead to selecting gold for both grating types and optimizing the bar thicknesses of the MEG and HEG gratings.

Because the grating bars are not opaque, the diffraction efficiency also depends on the cross-sectional shape of the bars, and this shape must be determined and incorporated into the model of the instrument performance. The effect of phase shifting is shown in Figure 3, where the dotted line represents the single-side first-order diffraction efficiency (i.e., one-half the total first-order diffraction efficiency) for a nonphased opaque grating, and the dashed and solid lines are from models that include the phase-shifting effects. For the opaque case (*dotted line*), the diffraction efficiency of the grating bars is constant

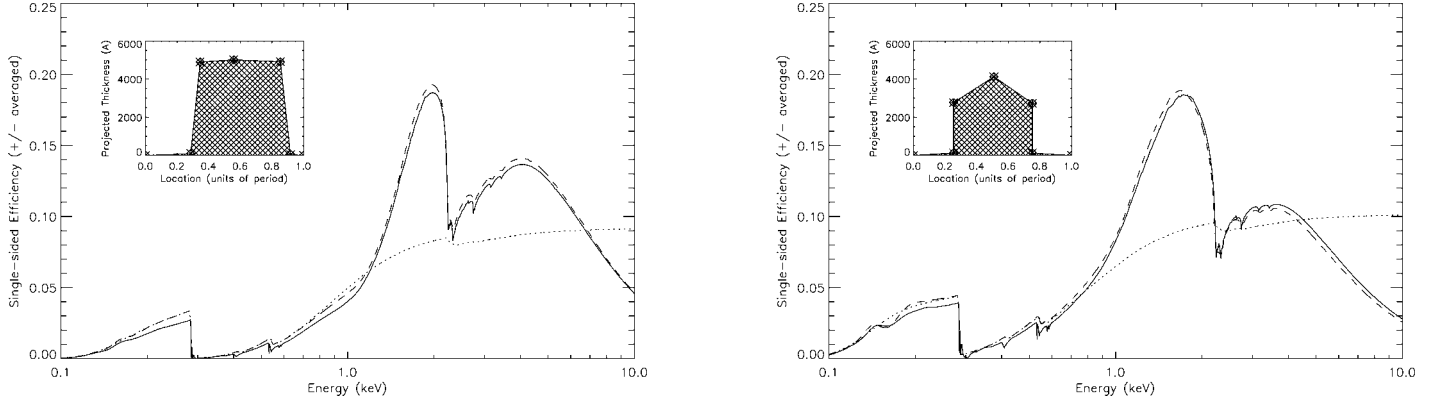


FIG. 3.—First-order diffraction efficiencies from example HEG (*left*) and MEG (*right*) multivertex models, plotted vs. energy (*solid curves*). The insets show the multivertex model grating bar cross-section. For reference, the efficiencies from a rectangular model are shown for the cases of a constant gold thickness (*dashed curve*) and the fully opaque case (*dotted curve*). The enhancement of the diffraction efficiency due to constructive phase shift, which occurs in the nonopaque cases (*solid and dashed curves*), is apparent above 1 keV. At very high energy, the nonopaque cases are introducing less phase shift, and the efficiency drops. Note also the subtle but significant differences between the multivertex efficiency (*solid curve*) and that of a similar thickness rectangular model (*dashed curve*). Effects of the polyimide and plating base layers are included and produce the low-energy fall-off and the carbon, nitrogen, oxygen, and chromium edges between 0.2 and 0.7 keV.

with energy; the variations seen in Figure 3 result from also including the absorption by the support membrane and the plating base (the thin base layers shown in Fig. 2), whose thicknesses are given in Table 1. These layers are nearly uniform over the grating and therefore only absorb X-rays.

The phased HEG and MEG gratings achieve higher efficiencies than opaque gratings over a significant portion of the energy band. The structure in the HEG and MEG efficiencies is caused by structure in the index of refraction of gold; i.e., the M edges around 2 keV. The efficiency falls at high energy as the bars become transparent and introduce less phase shift to the X-rays, falling below the opaque value at an energy depending on their thickness. The general formula for the efficiency of a periodic transmission grating, using Kirchhoff diffraction theory with the Fraunhofer approximation, is (Born & Wolf 1980, pp. 401–414)

$$g_m(\lambda) = (1/p^2) \times \left| \int_0^p dx \exp \{ ik[\nu(k) - 1]z(x/p) + i2\pi mx/p \} \right|^2, \quad (2)$$

where g_m is the efficiency in the m th order, k is the wave-number ($2\pi/\lambda$), $\nu(k)$ is the complex index of refraction, often expressed in real and imaginary parts (or optical constants) as $\nu(k) - 1 = -[\delta(k) - i\beta(k)]$, p is the grating period, and $z(\xi)$ is the grating path-length function of the normalized coordinate $\xi = x/p$. The path-length function $z(\xi)$ can be thought of as the projected thickness of the grating bar versus location along the direction of periodicity; at normal incidence, it is simply the grating bar cross-section.

The path-length function $z(\xi)$ can be reduced to a finite number of parameters. For example, if a rectangular bar shape is assumed, then z can be computed with two parameters, a bar width and a bar thickness (or height). Adding an additional parameter, Fischbach et al. (1988) reported on the theory and measurements of tilted rectangular gratings, which yields a trapezoidal path-length function for small incident angles. Our data are fit adequately for performance estimates if a simple rectangular grating bar shape is assumed (Schnopper et al. 1977; Nelson et al. 1994). However, modeling the measured first-order efficiencies to $\sim 1\%$ requires a more detailed path-length function. This is not surprising, given the evidence from electron microscope photographs (Fig. 9) that the bar shapes for the HETG gratings are not simple rectangles.

We found from laboratory measurements (see below) that sufficient accuracy could be achieved by modeling the grating bar shape in a piecewise linear fashion. We parameterize the shape by specifying a set of vertices (e.g., as shown in the insets of Fig. 3) by their normalized locations (ξ_j) and thicknesses [$z(\xi_j)$]; the endpoint vertices are fixed at (0, 0) and (1, 0). We have found in our modeling that five variable vertices are sufficient to accurately model these gratings in zeroth, first, and second orders and yet not introduce redundant parameters. Finally, this multivertex path-length function also lends itself to simple calculation, as presented in Appendix A.

Note that this multivertex model allows an asymmetric (effective) bar shape that generally leads to unequal plus and minus diffraction orders, as in the case of a blazed transmission grating (Michette & Buckley 1993) or as arises when a trapezoidal grating is used at off-normal (“tilted”) incidence. Hence, this multivertex model can be a useful extension of the

symmetric, multistep scheme formulation in Hettrick et al. (2004). For the HETG gratings, this asymmetric case arises primarily when the roughly trapezoidal HEG gratings were tested at nonnormal incidence, producing an asymmetry of up to 30% per degree of tilt. However, the asymmetry is linear for small tilt angles from the normal, and so the sum of the plus and minus order efficiencies remains nearly constant.

2.2. Synchrotron Measurements and Optical Constants

We used high-intensity X-ray beams at several synchrotron radiation facilities for several purposes: (1) to measure the optical constants and absorption edge structure of the grating materials and supporting polyimide membranes, (2) to make absolute efficiency measurements of several gratings to validate and constrain our grating performance model and provide estimates of its intrinsic uncertainties, (3) to calibrate several gratings for use as transfer standards in our in-house calibration, and (4) to measure the efficiencies of several gratings also calibrated in-house to assess uncertainties (see Flanagan et al. 1996, 2000). Synchrotron radiation tests were performed at four facilities over several years.

A first set of measurements were made at the National Synchrotron Light Source (NSLS) at Brookhaven National Laboratory (BNL), piggy-backing on equipment and expertise Graessle et al. (1996) developed to support the determination of the reflectivity properties of the HRMA coating. The general configuration of these tests is indicated in Figure 4; key ingredients are an input of bright, monochromatic X-rays from the beam line, a beam-monitoring detector that is inserted frequently to normalize the beam intensity, a detector fitted with a narrow slit (0.002 and 0.008 inches were used) that could be rotated to intercept radiation at a desired diffraction angle, and the grating itself, which could be rotated (“tilted”) about the vertical (grating bar) axis and also removed for detector cross-calibration. Data sets were taken automatically, with one or more of the controlled parameters varied: monochromator energy scan, diffraction angle (order) scan, and a grating tilt scan.

Initial modeling based on a rectangular grating bar model and using the optical constants δ and β obtained from the scattering factors (f_1, f_2) published by Henke et al. (1993) indicated significant disagreement with the Henke values for the gold optical constants (Nelson et al. 1994; Markert et al. 1995). The most noticeable feature was that the energies of the gold M absorption edges were shifted from the tabulated amounts by as much as 40 eV, a result obtained earlier by Blake et al. (1993) from reflection studies of gold mirrors. In an effort to determine more accurate optical constants, the transmission of a gold foil was measured over the range 2.03–6.04 keV, and the values of β and δ were revised (Nelson et al. 1994). The widely used Henke tables were modified in 1996 to reflect these results.

Subsequent tests on gratings explored bar shape, tilt, and

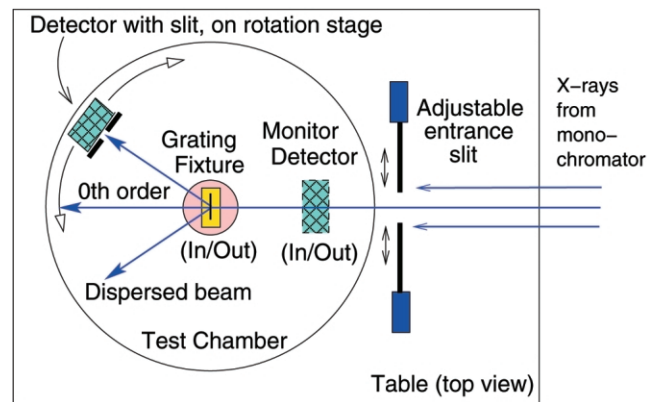


FIG. 4.—Measurement configuration at the National Synchrotron Light Source. X-rays from the beam line monochromator are incident from the right and are collimated by an entrance slit. A monitor detector can be quickly inserted to provide accurate normalization of the beam. The main detector measures the grating-dispersed X-ray flux and can be scanned in angle. (Adapted from Nelson et al. 1994.)

asymmetry (Markert et al. 1995), and tests at the radiometry laboratory of the Physikalisch-Technische Bundesanstalt (PTB) below 2 keV identified the need to accurately model the edge structures of the polyimide support membrane to improve the overall fit (Flanagan et al. 1996). The analysis of the tests of gold and polyimide membranes at PTB in 1995 October is detailed in Flanagan et al. (2000). In addition, cross-checks of the revised gold constants (above 2 keV) and polyimide were performed in 1996 August and November and have confirmed these latest revisions.

As a consequence of these analyses, our model now includes revised gold optical constants over the full energy range appropriate to the HETG, and detailed structure for absorption edges of polyimide, $C_{22}H_{10}O_4N_2$, and Cr. An example of the agreement between measured and modeled efficiencies is shown in Figure 5.

2.3. The Faceted Rowland Design

The HETGS optical design is based on an extension of the simple Rowland spectrometer design, in which the gratings and detector are located on opposite sides of an imaginary Rowland circle (Born & Wolf 1980). The Rowland configuration maintains the telescope focal properties in the dispersion direction for a large range of diffraction angle β , thereby minimizing aberrations. A detailed discussion of the physics of Rowland spectrometers (i.e., applying Fermat’s principle [Schroeder 1987] to evaluate aberrations of the faceted grating design) is given by Beuermann et al. (1978). What follows is a simplified, ray-based description of the basic design.

The “top view” of Figure 6 shows the plane of dispersion [the (x', y') plane], as viewed along the cross-dispersion di-

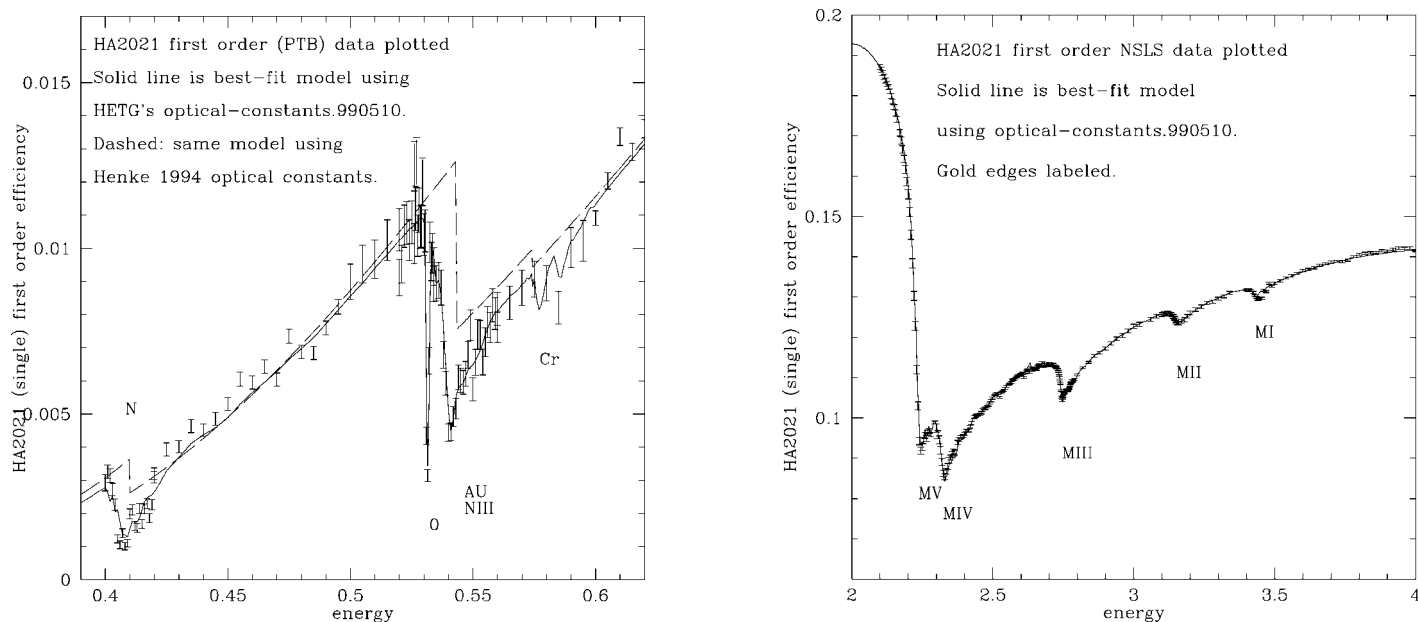


Fig. 5.—Synchrotron efficiency measurements. The first-order efficiency is generally smoothly varying, with energy in the HETGS band (see Fig. 4), except in the polyimide and Cr edge region (*left*) and the gold M edge region (*right*). The modeling process was driven by extensive sample measurements made with monochromatized synchrotron light sources. Shown here are the finely spaced measured data (*error bars*) with a best-fit multivertex model (*solid line*).

rection, z' . The diffraction angle is β , as defined by equation (1); note that the facet surfaces are normal to the incoming central X-rays and are thus not tangent to the Rowland circle. Through the geometric properties of the circle, rays diffracted from gratings located along the Rowland circle will all converge at the same diffracted point on the Rowland circle. The dotted lines represent zeroth-order ($m = 0$, $\beta = 0$) rays, and the solid lines show a set of diffracted-order ($m > 0$, $\beta > 0$) rays.

The bottom-panel “side view” gives a view along the dispersion direction y' at rays from a set of grating facets located in the (x', y') plane (the same three facets in the “top view” now seen in projection, shown in light shading), as well as additional grating facets (darker facets) located above (or equivalently below) the (x', y') plane. Each arc of additional facets is located on another Rowland circle obtained by rotating the circle in the top view about the rightmost line segment—the tangent to the Rowland circle that is parallel to the dispersion direction and passes through the zeroth-order focal point. The surface described by this rotation is the “Rowland torus.” As shown in the side view, all grating facets with centers located on this Rowland torus and with surfaces normal to the converging rays (*dotted lines*) will focus their diffracted orders on a common arc perpendicular to the (x', y') plane.

Together, these constructions show the astigmatic nature of the dispersed image: the rays come to a focus in the dispersion direction (the “Rowland focus”) at a location different from

their focus in the cross-dispersion direction (the “imaging focus”). This is demonstrated in the ray-trace example in Figure 7.

In order to maintain the best spectroscopic focus, the detector surface must conform to or approximate this Rowland curvature so that diffracted images are focused and sharp in the dispersion direction, and elongated in the cross-dispersion direction. The offset of the Rowland circle from the tangent at the zeroth-order focus is

$$\Delta X_{\text{Rowland}} = \beta^2 X_{\text{RS}}, \quad (3)$$

where X_{RS} is the Rowland spacing, the diameter of the Rowland circle.

At the Rowland focus (e.g., the $dx = 0$ case in Fig. 7), the image is elongated (blurred) in the cross-dispersion direction z' , due to the astigmatic nature of the focus, and has a peak-to-peak value given by

$$\Delta z'_{\text{astig}} = \frac{2R_0}{X_{\text{RS}}} \Delta X_{\text{Rowland}}, \quad (4)$$

where R_0 is the radius of the ring of gratings around the optical axis, as defined in Figure 6. The width of the image in the dispersion direction y' is given by a term proportional to the size of the (planar) grating facets that tile the Rowland torus. The peak-to-peak value of this “finite-facet size” blur is given

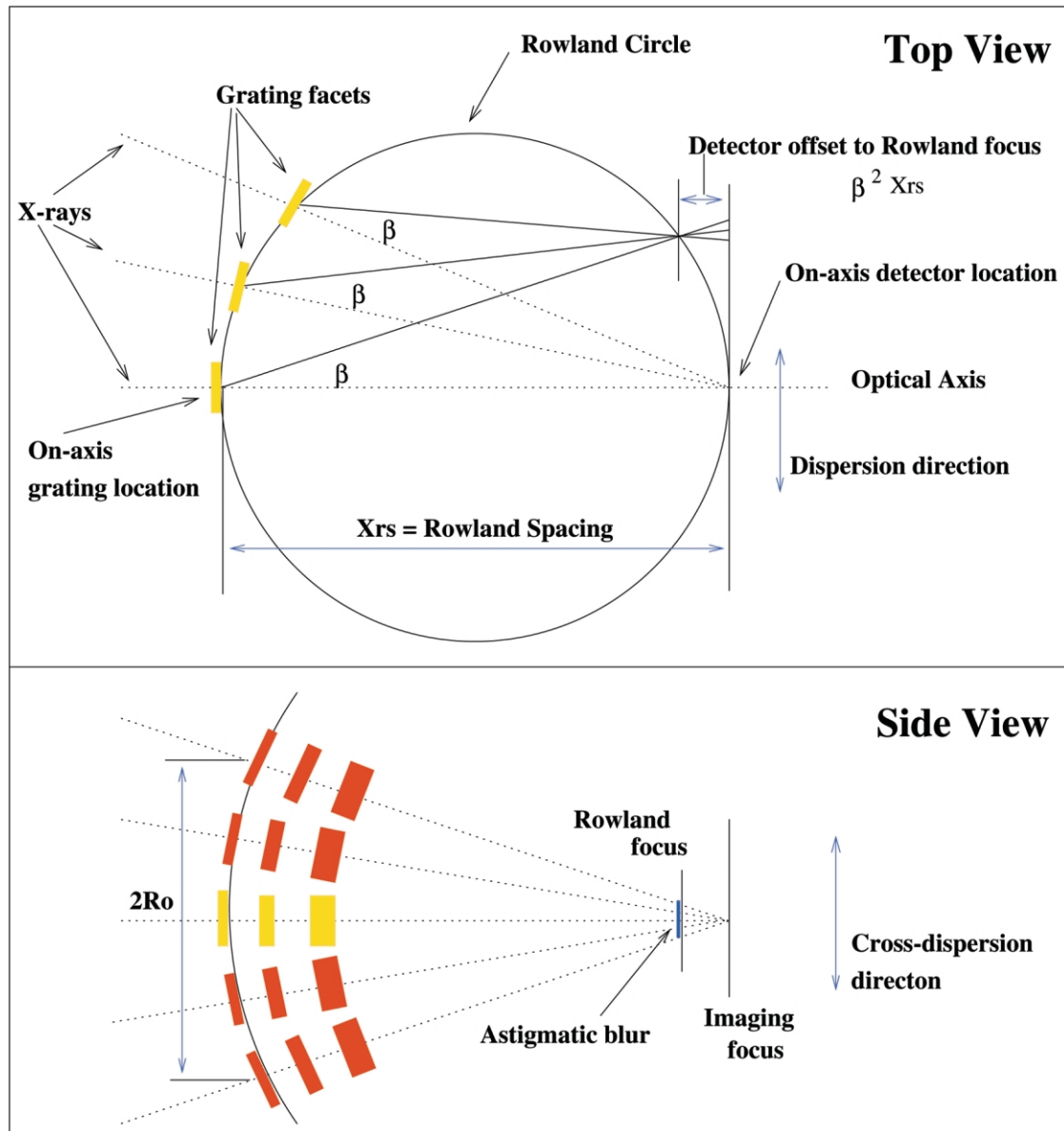


FIG. 6.—Simplified ray geometry for the Rowland torus design. The top view shows the spectrometer layout viewed from $+z$ (“above *Chandra*”), with the HRMA off the page to the left. X-rays reflected by the HRMA come to a focus at zero order (*dotted lines*). The grating facets diffract the rays into the m th-order spectra at angle β with respect to the optical axis, and bring the dispersed spectrum to a focus on the Rowland circle (*solid lines*). The Rowland spacing (X_{RS}) is the diameter of the Rowland circle and the distance from the gratings to the detector. In the side view, we see the cross-dispersion projection of the same rays. Notice that in the cross-dispersion direction, the diffracted rays focus behind the Rowland circle.

by

$$\Delta y'_{fr} = \frac{L}{X_{RS}} \left(R_0 \beta + \frac{\Delta X_{\text{Rowland}}}{2} \right), \quad (5)$$

where L is the length of a side of the square grating facet. This blur sets the fundamental resolving power limit for the Rowland design with finite-sized facets. For the HETGS design, this

contribution is much smaller than the ACIS pixel size (see the $dx = 0$ case of Fig. 7) and is negligible compared to the terms in the resolving power error budget of Appendix B.

3. HETG FABRICATION, TEST, AND ASSEMBLY

3.1. Facet Fabrication

The 144 HEG and 192 MEG grating facets are the key components of the HETG and presented major technical chal-

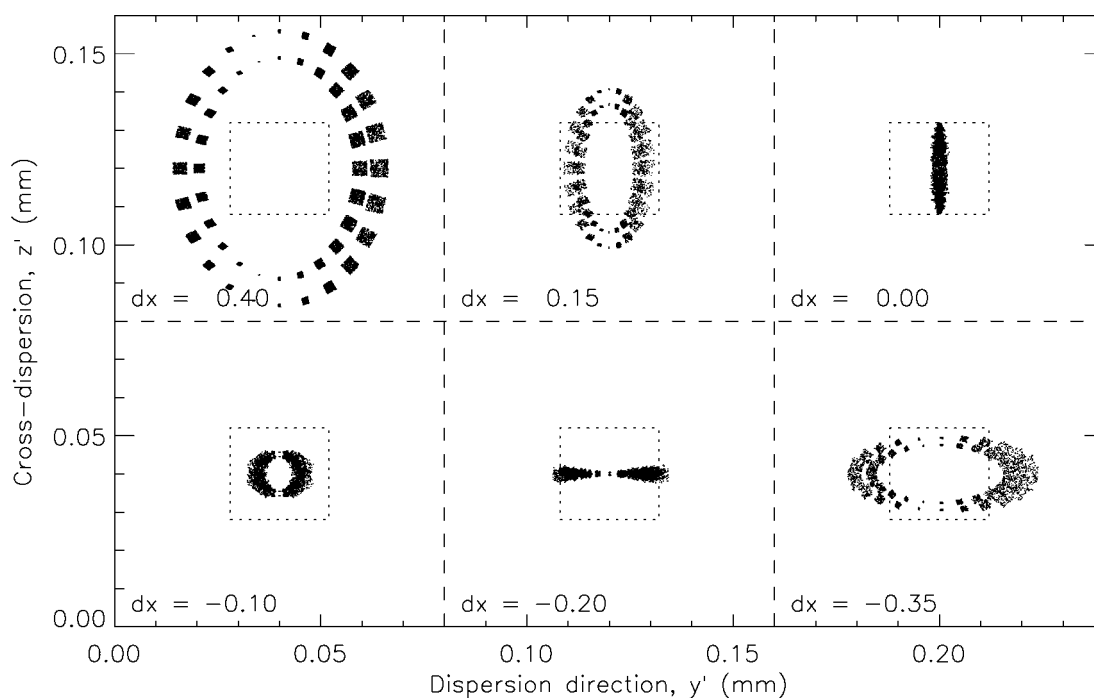


FIG. 7.—Ray trace of faceted Rowland geometry: 19 Å MEG images vs. defocus. The focal properties of the faceted Rowland design are demonstrated in this set of images at different defocus values, dx ; positive values are a displacement of the detector toward the grating. Parameters of the simulation approximate the MEG gratings on *Chandra* at a wavelength of 19 Å. At large defocus values ($dx = 0.40$ mm), the rays from each facet are visible; here there are 24 facets in each of two shells. The image comes to a minimum width in the dispersion direction at the Rowland focus ($dx = 0$) with a finite cross-dispersion width. At a defocus of $dx \approx -0.20$, the local detector surface is in the focal plane and the image is now well focused in the cross-dispersion direction. These spot diagrams were created by simple ray tracing of a perfect focusing optic combined with a faceted grating set; hence, the inherent astigmatism and finite facet-size blur of the Rowland design dominate the image at best focus ($dx = 0.0$). For reference, the dotted square is the size of an ACIS pixel.

lenges: to create facets with nanometer-scale periods, nearly rectangular bar shapes, nearly equal bar and gap widths, and sufficient bar depth to achieve high-diffraction efficiencies, and with a high degree of uniformity in all these properties within each facet and among hundreds of facets. The facets must also be sufficiently robust to withstand the vibrational and acoustic rigors of space launch without altering their properties, much less being destroyed.

The HETG grating facets were fabricated, one at a time, in an elaborate multistep process employing techniques adapted from those used to fabricate large-scale integrated circuits. Development work was initiated in the Nano Structures Laboratory, and the refinement of these processes took place over nearly two decades, with final flight production occurring in the Space Nanotechnology Laboratory of the (then) MIT Center for Space Research.

Each facet was fabricated on a silicon wafer, which was used as a substrate but did not form any part of the final facet. In brief, the process involved depositing the appropriate material layers on the wafer, imprinting the period on the outermost layer using UV laser interference, transferring that periodic pattern to the necessary depth, thereby creating a mold with the complement of the desired grating geometry, filling the

mold with gold, using electroplating, stripping away the mold material, etching away a portion of the Si substrate, aligning and attaching a frame, and then separating the finished facet from the silicon wafer. A highly simplified depiction of these steps is given in Figure 8 and is described below. More complete details of the fabrication process are available elsewhere (Schattenburg et al. 1994; Schattenburg 2001).

The first step (Fig. 8a) is to coat 100 mm diameter silicon wafers with six layers of polymer, metal, and dielectric, comprising either 0.5 μm (MEG) or 1.0 μm (HEG) of polyimide (which will later form the grating support membrane), 5 nm of chromium (for adhesion), and 20 nm of gold, which serve as the plating base, plus ≈ 500 nm of antireflection coating (ARC) polymer, 15 nm of Ta_2O_5 interlayer (IL), and 200 nm of UV imaging photopolymer (resist).

The second step (Fig. 8b) is to expose the resist layer with the desired periodic pattern of the final grating, using interference lithography at a wavelength of 351.1 nm. Two nearly spherical monochromatic wave fronts interfere to define the grating pattern period; the radii of the spherical wave fronts are sufficiently large to reduce the inherent period variation across the sample to less than 50 ppm rms. A high degree of period repeatability is required from the hardware, because a

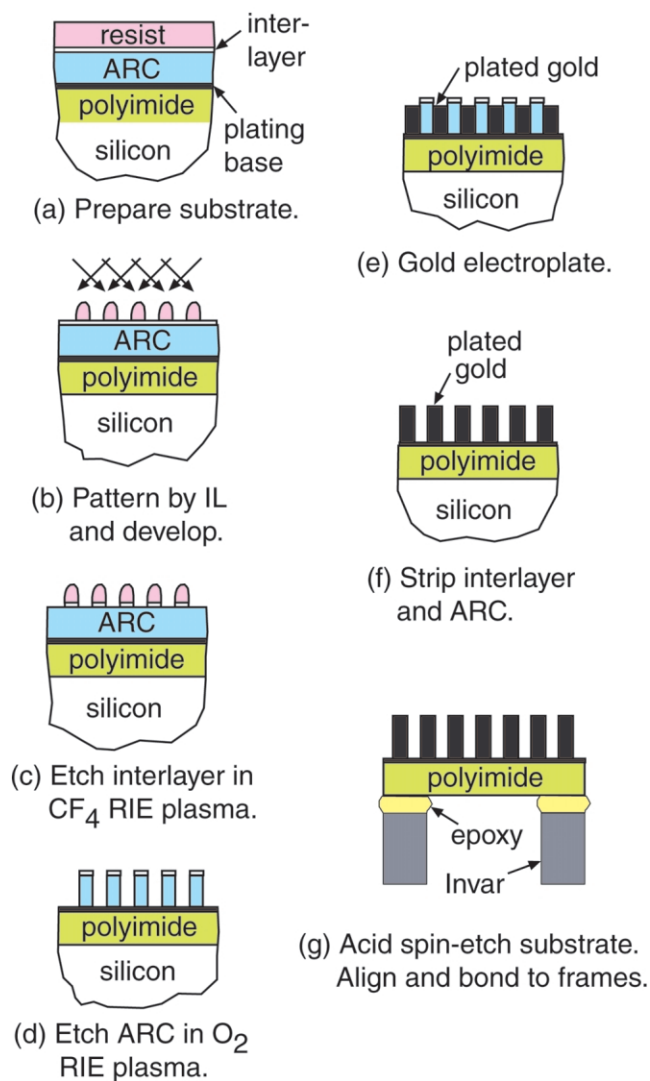
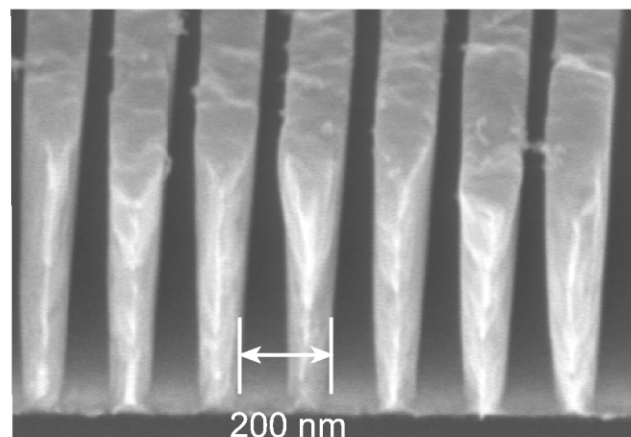
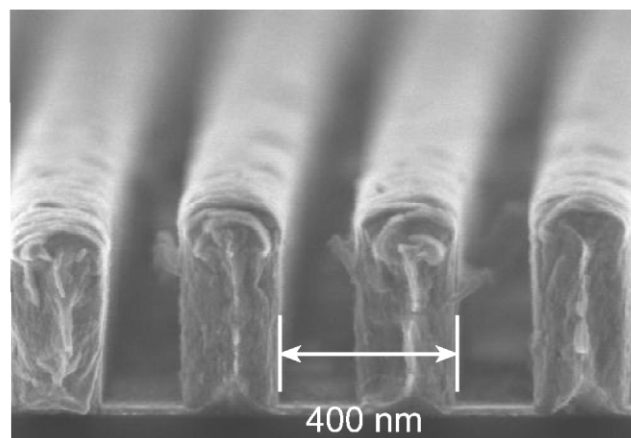


FIG. 8.—Simplified production steps for the HETG facets. The initial periodic pattern is created as the interference of two laser wave fronts. This pattern is etched into the polymer. Through electroplating, gold is deposited into the spaces between polymer bars. Removal of the polymer (stripping) and Si wafer support leaves the grating membrane in the wafer center. This membrane is then aligned and bonded to the Invar frame.

unique exposure is used for each grating facet of the HETG. Prior to each exposure, the moiré pattern between the UV interference standing waves and a stable reference grating fabricated on silicon was used to lock the interferometer period. A secondary interferometer and active control are used to ensure that the interference pattern is stable over the approximately 1 minute exposure time. The interlayer, ARC, and resist layers form an optically matched stack designed to minimize the formation of planar standing waves normal to the surface, which would compromise contrast and line-width control (Schattenburg et al. 1995).



(a) High Energy Grating (HEG).



(b) Medium Energy Grating (MEG).

FIG. 9.—Electron micrographs of representative HEG and MEG grating bars.

In the third step (Fig. 8c), the resist pattern is transferred into the interlayer using CF_4 reactive-ion plasma etching (RIE). In the fourth step (Fig. 8d), the IL pattern is transferred into the ARC using O_2 RIE. The RIE steps are designed to achieve highly directional vertical etching with minimal undercut.

The fifth step (Fig. 8e) is to electroplate the ARC mold with low-stress gold, which builds up from the Cr/Au plating base layer. The sixth step (Fig. 8f) is to strip the ARC/IL plating mold using a hydrofluoric (HF) acid etch and plasma etching with CF_4 and O_2 . At this point, the gold grating bars are complete; Figure 9 shows electron micrographs of cleaved cross-sections of the gratings.

In the last step (Fig. 8g), a circular portion of the Si wafer under the grating and membrane is etched through from the back side in HF/ HNO_3 acid, using a spin-etch process that keeps the acid from attacking the materials on the front side (Schattenburg et al. 1995). The membrane, supported by the remaining ring of unetched Si wafer, is then aligned to an

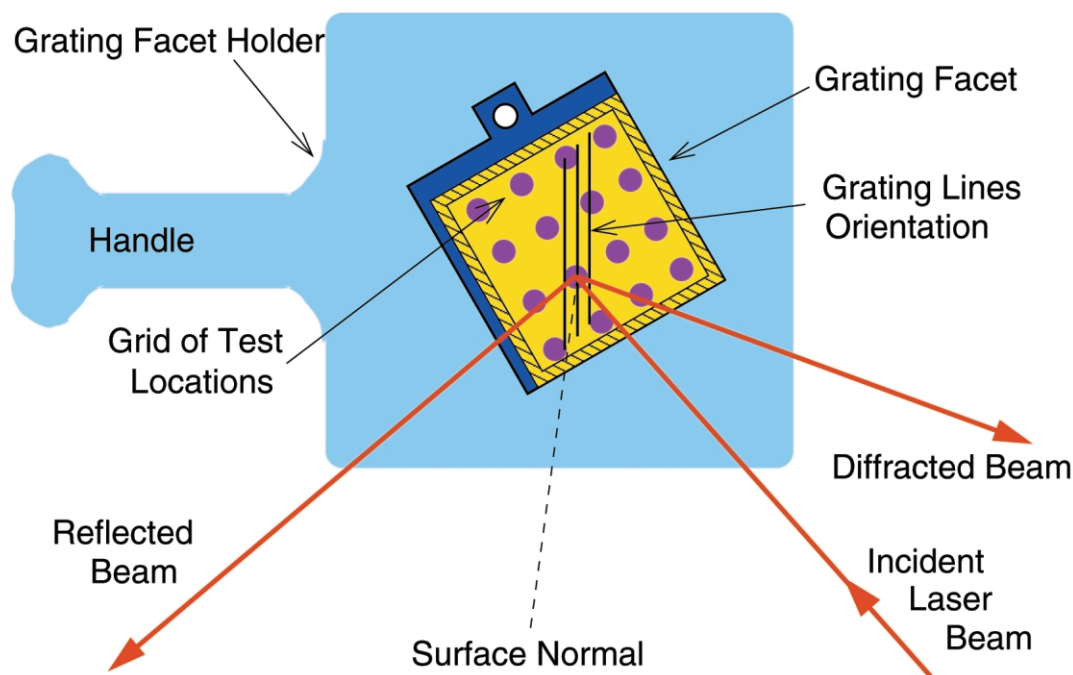


FIG. 10.—Laser reflection (LR) principle of measurement. Note that during this and other laboratory testing, the flight grating is not directly handled; the *nonflight* grating facet holder serves as interface to both humans and equipment.

angular tolerance of $\leq 0.5^\circ$ and bonded to a flight “frame” using a two-part, low-outgassing epoxy. Once cured, the excess membrane and Si ring is cut away from the frame with a scalpel. The frames are custom made of black chrome-plated Invar 36, which is machined to tight tolerances, and the membrane-bonding faces were hand lapped to remove burrs and ensure a flat, smooth surface during bonding. The use of Invar reduces any grating period variations that might be caused by thermal variation of the HETG environment between stowed and in-use positions on *Chandra*. Likewise, the frame design has a single mounting hole to reduce the effect of mounting stresses on the facet period. Each completed facet was mounted in a nonflight “holder” to allow for ease in storing, handling, and testing (a schematic of the holder and facet is shown in Fig. 10).

After years of preparation, we fabricated 245 HEG and 265 MEG gratings in 21 lots over a period of 16 months. Tests on the individual facets (§ 3.2) were used to select the elite set of 336 flight grating facets. As a postscript to the fabrication of the *Chandra* HETG facets, we note that we have since extended our technology (Schattenburg 2001) to fabricate gratings with finer periods (Savas et al. 1996), mesh-supported “free-standing” gratings for UV/EUV and atom-beam diffraction and filtering (van Beek et al. 1998), and supersmooth reflection gratings (Franke et al. 1997).

3.2. Facet Laboratory Tests and Calibration

The completed HETG facets were put through a set of laboratory tests to characterize their quality and performance and

to enable the selection of an optimal complement of flight gratings. Each facet went through a sequence of tests: (1) visual inspection, (2) laser reflection (LR) test 1, (3) acoustic exposure, (4) LR test 2, (5) thermal cycling, (6) LR test 3, and finally (7) X-ray testing. As noted, to reduce direct handling, each fabricated facet was mounted to its own aluminum holder, and the facet-level test equipment was designed to interface with the holder.

The LR test (Dewey et al. 1994) uses optical diffraction of a laser beam (HeNe 633 nm for MEG, HeCd 325 nm for HEG) from the grating surface to measure period and period variations of each facet. As shown in Figure 10, the laser beam is incident on the grating undergoing testing at an off-normal angle. A specularly reflected beam and a first-order-diffracted beam emerge from the illuminated region of the grating. These beams are focused with simple, long focal length (≈ 500 mm) lenses onto commercial CCDs. Under computer control, the grating is moved so that a raster of over 100 regions is illuminated, and the centroids of the reflected and diffracted beams in the CCD imagers are measured and recorded. Changes in the four CCD spot coordinates (X_{ref} , Y_{ref} , X_{diff} , and Y_{diff}) are linearly related to changes in four local grating properties: the grating surface tilt and tip, the grating period, and the grating line orientation (roll). These measurements are referenced to gratings (HEG and MEG) on silicon substrates permanently mounted in the system and measured before and after each raster scan set. The LR data files are used to determine for each grating facet a mean period p and an rms period variation

dp/p , as well as contours of period variation across the facet. The flight grating sets were then selected to achieve minimal overall period variation for the complete HEG and MEG arrays (106 and 127 ppm rms, respectively). The ability of the LR apparatus to measure absolute period was calibrated using samples on silicon measured independently at the National Institute for Standards and Technology. The average periods of the grating sets as determined from the LR measurements are given in Table 1 (HETG Laboratory Parameters).

The diffraction efficiency (Dewey et al. 1994) of each facet was measured using the X-Ray Grating Evaluation Facility (X-GEF), consisting of a laboratory electron-impact X-ray source, a collimating slit and grating assembly, and two detectors (a position-sensitive proportional counter and a solid-state detector) in a 17 m long vacuum system. Facet tests were conducted at a rate of two gratings per day. The zeroth- and ± 1 st and ± 2 nd-order efficiencies were measured for five swathlike regions on each facet, and at up to six energies (Cu L 0.930 keV, Mg K 1.254 keV, Al K 1.486 keV, Mo L 2.293 keV, Ti K 4.511 keV, and Fe K 6.400 keV). Two facets that had been tested at synchrotron facilities (Markert et al. 1995) served as absolute efficiency references. The measured monochromatic efficiencies were fit with our multivertex efficiency model (Flanagan et al. 1995); an example model fit to X-GEF measured points is shown in Figure 11. These measurements and models allowed us to select the highest efficiency gratings for the flight HEG and MEG sets, and also to predict the overall grating-set efficiencies (§ 4.2).

The HETG flight-candidate gratings were X-GEF tested from mid-1995 through September of 1996 at a typical rate of two per day. A small set of nonflight gratings were retained in a laboratory vacuum, and their diffraction efficiencies were measured with X-GEF at seven epochs from late 1996 to 2003 February. These “vacuum storage gratings” showed no evolution in their diffraction properties, giving us an expectation of stability for the HETG efficiency calibration.

3.3. HETG Assembly

The flight HETG came into being when the 336 flight grating facets selected were mounted to the HETG Element Support Structure (HESS). The HESS was numerically machined from a single plate of aluminum ≈ 4 cm thick (Pak & McGuirk 1994; Markert et al. 1994) to create a spoke-and-ring structure with mounting surfaces and holes for the facets that conformed to the Rowland torus design, with a diameter given in Table 1. The HESS mechanical design using tapered ≈ 6 mm thick spokes achieves several objectives: a low weight, an accurate positioning of the facets, and the ability to withstand the high launch vibration environment. The flight HETG is shown in Figure 12, where the HESS is black and the facet surfaces are gold; its outer diameter is 1.1 m, and three attachment points provide for its mounting to one of the two *Chandra* telescope grating insertion mechanism yokes. The completed flight

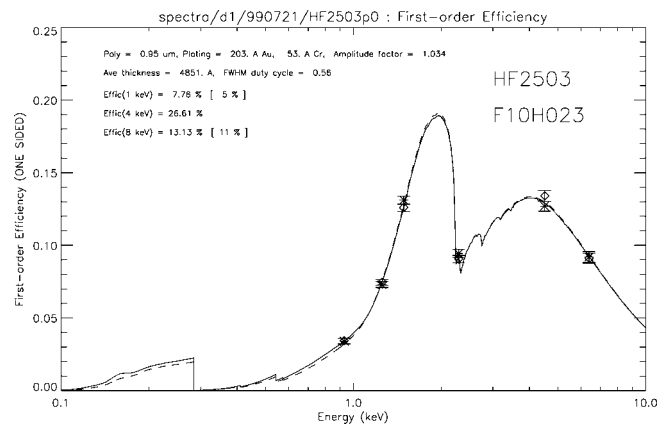


FIG. 11.—Example of X-GEF measurements and model fit. The measured plus and minus first-order efficiencies at the six test energies are shown by the symbols with error bars; also plotted are the first-order efficiencies of the best-fit multivertex model (solid and dashed curves, respectively). Second and zeroth-order measured efficiencies (not shown) have also been included in the model fit.

HETG weighs 10.41 kg, of which 8.88 kg is due to the HESS structure, 1.21 kg for the grating elements, and 0.32 kg for the element-to-HESS mounting hardware. The “active ingredient” of the HETG, the gold grating bars, weighs a meager 1.14 mg.

The single-screw mounting scheme used to attached the facets to the HESS adequately fixes all degrees of freedom of the facet, except for rotation around the screw axis; i.e., the “roll” angle of the facet. The roll angle was aligned using the ability of the grating to polarize transmitted light, which has a wavelength longer than the grating period. A schematic of our setup, based on the polarization alignment technique of Anderson et al. (1988), is shown in Figure 13. Light from the HeNe laser passes through a photoelastic modulator at a 45° angle. The emerging beam can be viewed as having two linearly polarized components at right angles, with a time-dependent relative phase varying as $\sin(\omega t)$. Ignoring any effect of the polyimide on the light, the polarizing grating bars transmit only the projection of these components that is perpendicular to the bars. For a nonzero θ_g , some fraction of each of the modulator-axes components is transmitted, resulting in interference and an intensity signal at 2ω proportional to θ_g . This measurement setup was used along with appropriate manipulation fixturing to set each facet to its desired roll orientation (differing by $\approx 10^\circ$ between HEG and MEG facets) with, in general, an accuracy better than $1'$.

When all facets were aligned and the alignment rechecked, they were then epoxied to the HESS. The flight HETG was then subjected to a random vibration test. Once again, the alignment apparatus was used to make a set of measurement of the facet roll angles. These final measurements indicated that all gratings were held secure and the roll variation was $0'.42$ rms averaged over all gratings, with less than a dozen facets having

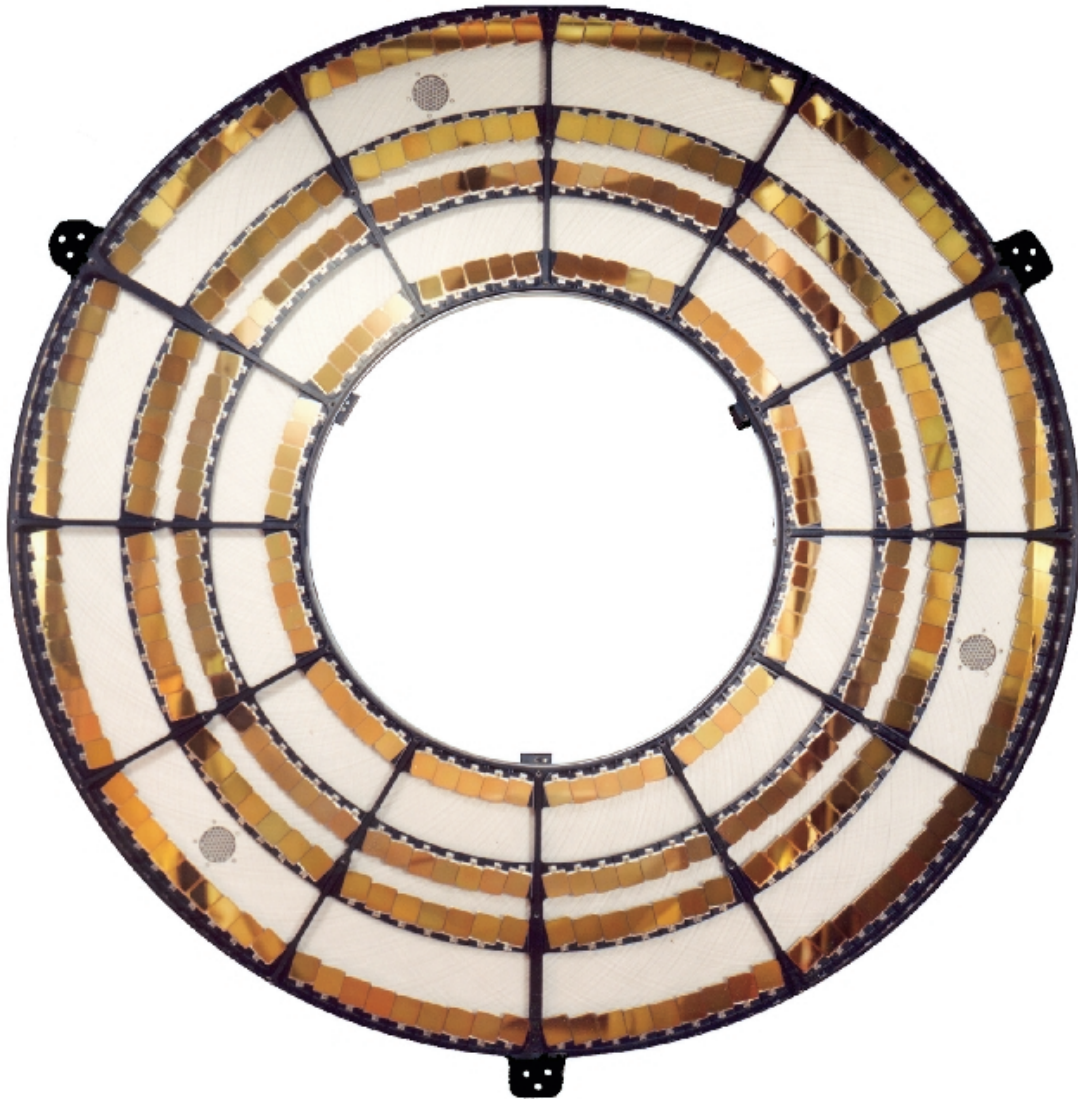


FIG. 12.—Photograph of the HETG. Glittering gold, the 336 grating facets are visible mounted to the black anodized support structure, the HESS. The outer two rings of gratings are MEGs and intercept rays from the HRMA shells 1 (*outermost*) and 3; the inner two rings are HEGs and work with HRMA shells 4 and 6 (*innermost*).

angular offsets in the 1° – 2° range. During subsequent full-up ground calibration using X-rays (§ 4), we discovered that in fact the roll angles of six of the MEG facets showed improper alignment well outside of this range.

4. PREFLIGHT PERFORMANCE TESTS AND CALIBRATION

The *Chandra X-Ray Observatory* components that are most relevant to flight performance were tested at the NASA Marshall Space Flight Center X-Ray Calibration Facility (XRCF) in Huntsville, Alabama, from late 1996 through spring of 1997

(Weisskopf & O'Dell 1997; O'Dell & Weisskopf 1998). These full-up tests provided unique information on the HETG and its operation with the HRMA and ACIS. Key results of this testing are summarized here; details of the analyses are in the cited references and the HETG Ground Calibration Report.²

With the test X-ray sources (Kolodziejczak et al. 1995) located at a finite distance from the HRMA (518 m), the HRMA focal length at XRCF was longer by ≈ 200 mm than the expected flight value. In order to optimally intercept the rays

² Available at the HETG Web page, <http://space.mit.edu/HETG/report.html>.

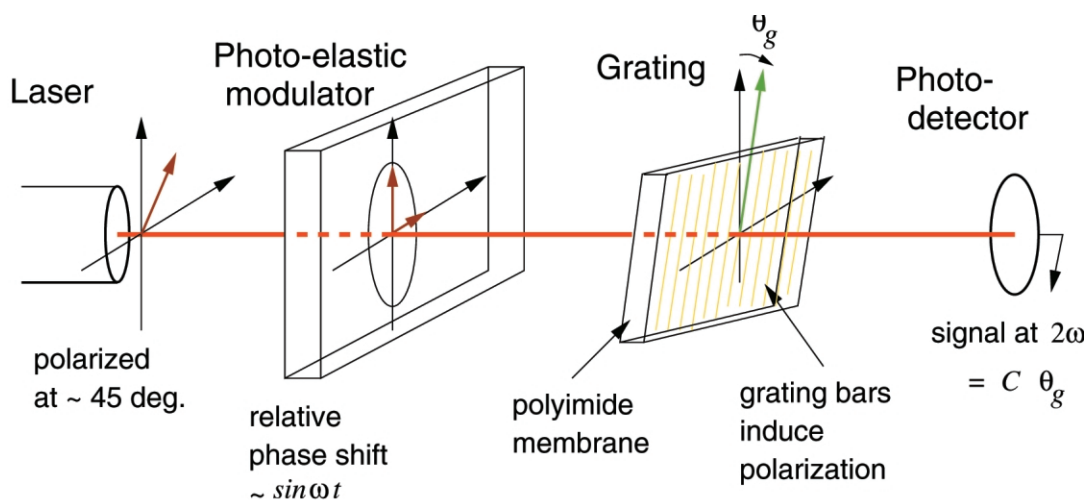


FIG. 13.—Schematic of the polarization alignment setup. The intensity of the detected interference signal at 2ω is proportional to θ_g for small angles. Note that in this configuration the polyimide membrane is between the modulator and analyzer (the grating bars); hence, the polarization/phase properties of the membrane can effect the measurement result.

exiting the HRMA hyperboloid at XRCF, the HETG Rowland spacing—that is, the distance from the HRMA focus to the HETG effective on-axis location—was increased by ≈ 150 mm over its design value (Table 1). We evaluated the effect of this difference between the as-machined Rowland diameter (X_{HESS}) and the as-operated Rowland spacing ($X_{\text{RS, XRCF}}$) using our ray-trace code. This let us set the scale factor for a simple analytic estimate of the rms dispersion blur:

$$\sigma_z \approx 0.2R_0^2 \frac{\lambda}{p} \left(\frac{1}{X_{\text{HESS}}} - \frac{1}{X_{\text{RS, XRCF}}} \right), \quad (6)$$

Using extreme-case values ($R_0 = 500.0$ mm, $\lambda = 40$ Å, and $p = 4000$ Å), this equation gives an additional blur of an order of $1 \mu\text{m}$ rms; insignificant compared to the image rms, which is greater than $15 \mu\text{m}$ rms.

In addition to the HETG spacing difference, other aspects of the XRCF testing differed from flight conditions. The HRMA, which was designed to operate in a $0 g$ environment, was specially supported and counterbalanced to operate in $1 g$. This results in a mirror point-spread function (PSF) that is not identical to the PSF expected in flight. A nonflight shutter assembly allowed quadrants of the HRMA shells to be vignetted as desired. Among other things, this allowed the HEG and MEG zeroth orders to be measured independently. In addition to the flight detectors, ACIS, and the High Resolution Camera (HRC; Murray et al. 1998), several specialized detectors were used to conduct the tests.

4.1. Line Response Function Measurements

Detailed images and measurements of HETG-diffracted X-ray lines were made at XRCF to study the LRF (Marshall et al. 1997). For example, Figure 14 shows an image and resulting spectrum of the MEG third-order diffracted Al K line complex recorded at XRCF with the nonflight High Speed Imager (HSI) microchannel plate detector. Measurements of various parameters related to the LRF are described in the following paragraphs and summarized in Table 1.

4.1.1. Grating Angles

By measuring the centroid of the diffracted images from HEG and MEG gratings, the opening angle between HEG and MEG was measured to be very close to the 10° design value (see Table 1).

4.1.2. Grating Period and Rowland Spacing

Measurements using X-ray lines of known wavelength were used to confirm the values of the grating periods and measure the HETG Rowland spacing at XRCF. The ratio of HEG to MEG period determined from measurements agrees within a 100 ppm uncertainty, with the ratio expected based on the lab-derived periods in Table 1. Adopting these periods and an Al K energy of 1.4867 keV, the HETG Rowland spacing as-operated at XRCF was determined and is given in Table 1.

4.1.3. LRF Core Measurements

In order to see if the insertion of the HETG modified the zeroth-order image, HSI exposures were taken in Al K X-rays of each shell of the HRMA, illuminated in turn, with no grating

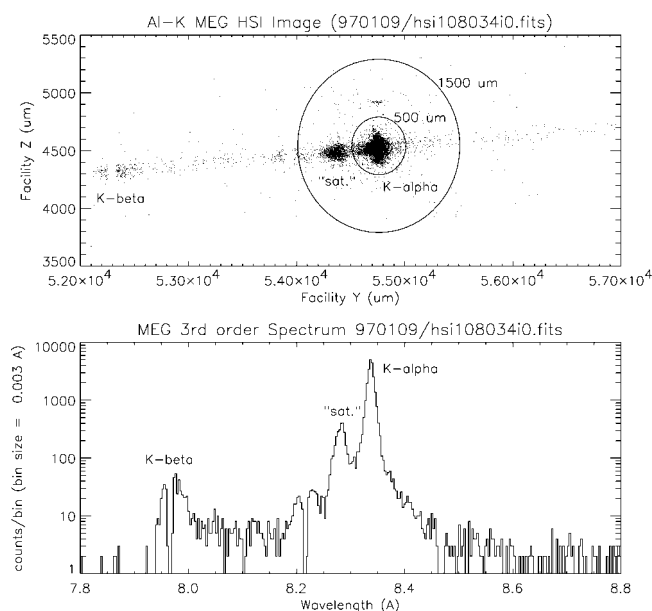


FIG. 14.—XRCF image of third-order MEG Al K line (*top*) and the resulting grating-produced spectrum (*bottom*). A strong “satellite” line is clearly visible near the $K\alpha$ peak. This image was obtained with the high-speed imager (HSI) in the focal plane; its instrumental gaps have not been removed (e.g., at the $K\beta$ line). Note the misaligned MEG grating outlier at Facility z of ≈ 4900 ; the extent in the z -direction of the main image is due to several more misaligned MEGs.

present. With the HETG, inserted images were obtained for the zeroth order of the MEG-only and HEG-only through each of four quadrants. The HRMA exposures for shells 1 and 3 (4 and 6) were then compared with the combined MEG (HEG) zeroth-order quadrant images. Comparing the projections of the two data sets binned to $10\ \mu\text{m}$ shows good agreement in shape, within 10%–20% in each bin, over two decades of the PSF intensity, covering the spatial range $\pm 150\ \mu\text{m}$. In particular, the inner core of the HRMA PSF at XRCF shows a FWHM of $\approx 42\ \mu\text{m}$, and insertion of the HETG adds no more than an equivalent FWHM of $\approx 20\ \mu\text{m}$; i.e., at most, increasing the FWHM from 42 to $46\ \mu\text{m}$.

For diffracted images, precise measurements were made of the core of the PSF by using slit scans of the Mg K 1.254 keV ($9.887\ \text{\AA}$) line in the bright orders $m = 0, 1,$ and 2 for HEG, and $m = 0, 1,$ and 3 for MEG. Scans were made along both the dispersion and cross-dispersion directions using 10 and $80\ \mu\text{m}$ wide slits in front of proportional counter detectors. To create simulated XRCF slit-scan data, a spectral model of the XRCF source was folded through a MARX (Wise et al. 2000) ray-trace simulation tailored to XRCF parameters that affect the intrinsic LRF (most importantly, finite source distance, finite source size, and an additional $0'.3$ of HRMA blur). The intrinsic FWHM of the line spectral model and the period variation dp/p values for each grating type (HEG and MEG) were

then adjusted in the simulation. Good agreement with the XRCF data is obtained when the core of the Mg K line is modeled as a Gaussian with an $E/dE = 1800$, the HEG gratings have a dp/p value of $146\ \text{ppm rms}$, and the MEG gratings have a dp/p of $235\ \text{ppm rms}$. These values are larger than expected from the individual LR results and likely represent slight additional distortions introduced during the facet-to-HESS alignment and bonding process. However, they are within our design goal of $250\ \text{ppm}$.

4.1.4. Misaligned MEG Gratings

As seen and noted in Figure 14, a small “ghost image” is visible in the cross-dispersion direction “above” the diffracted Al K line. Analyzing similar images taken quadrant by quadrant, as well as a very ($65.5\ \text{mm}$) defocused image of the MEG third order, which isolated the individual grating facet images (Marshall et al. 1997), we were able to demonstrate that this and other ghost images closer to the main image were created by individual MEG grating facets whose grating bars are “rolled” from the nominal orientation. In all, six of the 192 MEG facets have roll offsets in the range of $3'$ to $25'$ —greatly in excess of the laboratory alignment system measurement results. The individual facets were identified, and all came from fabrication lot 7—the only lot that was produced with prototype fabrication tooling during the membrane mounting step (Fig. 8g). It was subsequently demonstrated in the laboratory (by R. Elder) that inserting a stressed polyimide membrane between the photoelastic modulator and the grating (see Fig. 13) could create a shift in the alignment angle of an order of arcminutes, and which varied with applied stress. Note in Figure 13 that the polyimide layer of the facet being aligned is in the optical path between the polarization modulated alignment laser and the grating bars. This clearly suggests that stress birefringence (Born & Wolf 1980, p. 703) in the grating’s polyimide membrane introduces unintended bias offsets in the optical measurement of the grating bar angles, effectively causing their misalignment by these same bias angles.

4.1.5. Roll Variations

Mg K slit scans, described above, were also taken in the cross-dispersion direction and provide a check on the roll variations and alignment of the grating facets, the main contributor to cross-dispersion blur beyond the mirror PSF and Rowland astigmatism. Cross-dispersion distributions were input to the ray-trace simulations and adjusted to agree with the data. The resulting HEG and MEG roll distributions each have an rms variation of $1/8$. The MEG distribution is close to Gaussian, while the HEG shows a clear two-peaked distribution, with the peaks separated by $3'$. These variations are larger than the $0'.42$ rms value expected from the polarization alignment laboratory tests. The most likely cause is polyimide membrane effects similar to those that produced the misaligned MEGs, but oc-

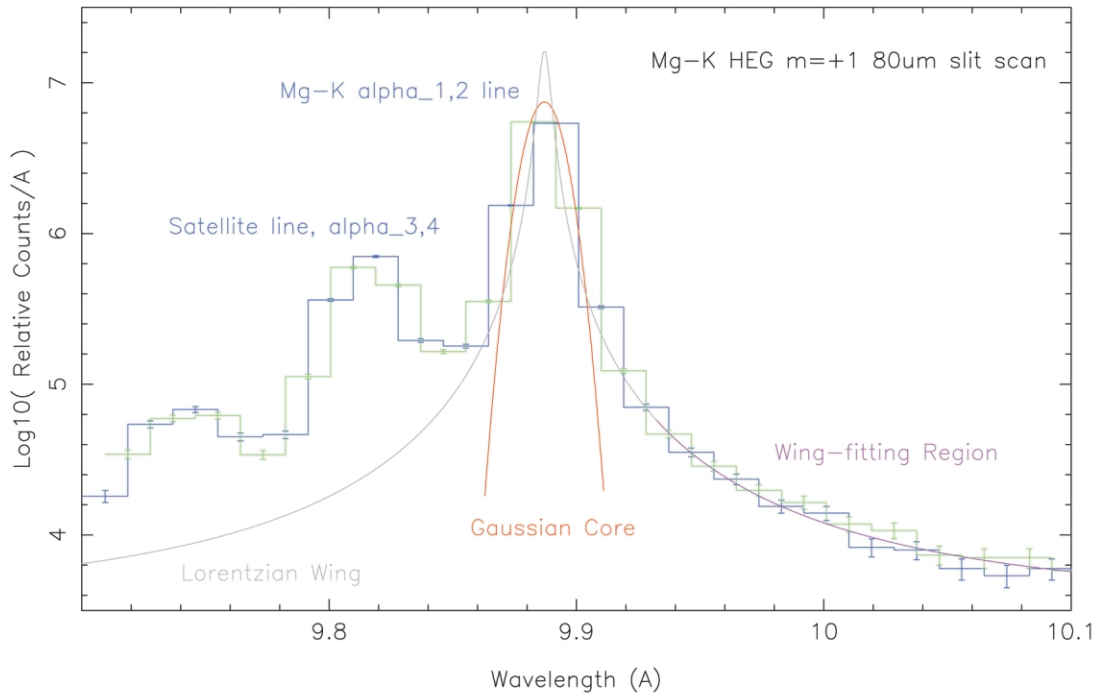


FIG. 15.—Wings of the LRF. At XRCF a focal-plane proportional counter with an $80 \times 500 \mu\text{m}$ aperture was scanned across the dispersed Mg K line image; two interleaved scans (offset by $40 \mu\text{m}$) of the HEG $m = +1$ order are shown here. To measure the wing level, the core of the LRF is fit with a Gaussian, and a region in the wings is fit with a Lorentzian; these fit parameters are used to quantify the wing level. Most of the wing flux seen here is due to the natural Lorentzian line shape of the Mg K line, and not the HETGS instrument.

curing at a lower level. The misaligned gratings and the roll distributions are explicitly modeled in MARX simulations.

4.1.6. Wings on the LRF

Wide-slit scans of the Mg K line were used to set an upper limit to any “wings” on the LRF introduced by the HETG gratings. The Mg K PSF was scanned by an $80 \times 500 \mu\text{m}$ slit for the MEG and HEG mirror shell sets separately. These scans were fit using ISIS (Houck & DeNicola 2000) software, by a Gaussian in the core and a Lorentzian in the wings, as shown in Figure 15. Quantitatively, the wing level away from the Gaussian core can be expressed as

$$L_w(\Delta\lambda) = A_G C_{\text{wing}} / (\Delta\lambda)^2, \quad (7)$$

where L_w is the measured wing level in counts \AA^{-1} , A_G is the area of the Gaussian core in counts, and $\Delta\lambda = \lambda - \lambda_0$ is the distance from the line center. The strength of the wing is given by the value C_{wing} , which has units of “fraction/ $\text{\AA} \times \text{\AA}^2$,” or (more opaquely) just “ \AA .” Using this formalism, the observed wing levels were determined for the HEG first and second orders and the MEG first and third orders, giving values of 8.6×10^{-4} , 7.1×10^{-4} , 12.2×10^{-4} , and $7.8 \times 10^{-4} \text{\AA}$, respectively. Of these totals, 5.6×10^{-4} is due to the intrinsic Lor-

entzian shape of the Mg K line itself (Agarwal 1991, p. 108), with the reasonable value of a natural line width of 0.0035\AA . The remaining wing level can be largely explained as due to the wings of the HRMA PSF itself: because the LRF is essentially the HRMA PSF displaced along the dispersion direction by the grating diffraction, wings of the mirror PSF directly translate into wings on the grating LRF. Subtracting these values, we get an estimate of (upper limit on) the contribution to the wing level by the HEG and MEG gratings per se (as given in Table 1).

4.1.7. Scatter Beyond the LRF

Tests were also carried out at XRCF to search for any response well outside of the discrete diffraction orders. A high-flux monochromatic line was created by tuning the Double Crystal Monochromator (DCM) to the energy of a bright tungsten line from the rotating anode X-ray source. The HEG grating set did show anomalous scattering of monochromatic radiation (Marshall et al. 1997); in particular, a small flux of events with significant deviations from the integer grating orders are seen concentrated along the HEG dispersion direction (Fig. 16). No such additional scattering is seen along the MEG dispersion direction.

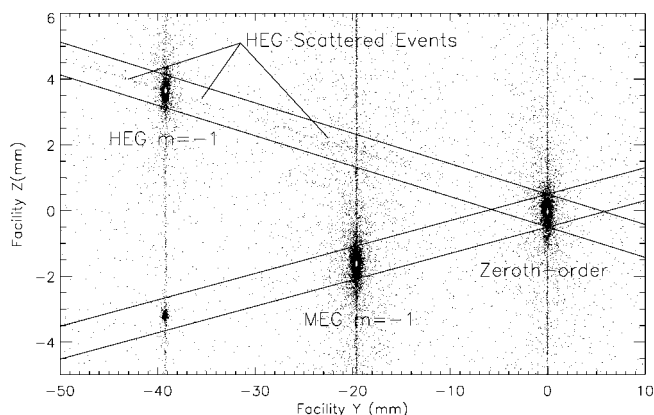


FIG. 16.—Scattered events seen in a monochromatic exposure at XRCF. The XRCF Double Crystal Monochromator was tuned to the tungsten 1.3835 keV line for this HETG-ACIS-S exposure. HEG scattered events are clearly visible concentrated along the HEG dispersion direction on either side of the HEG first-order region and near the one-half-order region. In contrast, the MEG shows few if any such events, nor are such events seen near zeroth order from either grating.

The origin of this scattering was understood using as an approximate model a grating with rectangular bars that incorporates spatially correlated deviations in the bar parameters (Davis et al. 1998); i.e., there is Fourier power in the grating structure at spatial periods other than the dominant grating period and its harmonics. Expressions for the correlations and the scattering probability were derived and then fit to the experimental data. The resulting fits, while not perfect, do reflect many of the salient features of the data, confirming this as the mechanism for the scattering. The grating bar correlations deduced from this model lead to a simple physical picture of grating bar fluctuations in which a small fraction of the bars (0.5%) have correlated deviations from their nominal geometry, such as a slight leaning of the bars to one side. It is reasonable that the HEG gratings, with their taller, narrower bars, are more susceptible to such deviations than the MEG, which does not show any measurable scatter.

In practice, the scattered photons in HEG spectra are excluded from analysis through order selection using the intrinsic energy resolution of ACIS: the energy of the scattered photon is significantly different from the energy expected at its apparent diffraction location. This is not true for scattered events that are close to the diffracted line image, and they will make up a local low-level pedestal to the HEG LRF. However, the power scattered is small compared to the main LRF peak, generally contributing less than 0.01% of the main response into a 3 FWHM wide region (0.036 Å) and less than 1% in total.

4.1.8. ACIS Rowland Geometry

An XRCF test was designed to verify the Rowland geometry of the HETGS; in particular, that all diffracted orders simul-

taneously come to best focus in the dispersion direction. Data were taken with each of four quadrants of the HRMA illuminated, allowing us to determine the amount of defocus for each of the multiple orders imaged by the detector. Because of the astigmatic nature of the diffracted images, the axial location of “best focus” depends on which axis is being focused. The results of this test (Stage & Dewey 1998) were limited by the number of events collected in the higher orders. However, it was concluded that (1) the astigmatic focal property was confirmed, (2) the HEG and MEG focuses at XRCF differed by 0.32 mm, as expected from HRMA modeling, and (3) the ACIS detector was tilted by less than 10' about the z -axis.

4.2. Efficiency and Effective Area Measurements

A major objective of XRCF testing was to measure the efficiency of the fully assembled HEG and MEG grating sets and the effective area of the full HRMA+HETG+ACIS system. The HETGS effective area or ARF (Davis 2001a) for a given grating set or *part*, indicating HEG or MEG, and diffraction order m can be expressed in simplified form as

$$A_{p,m}(\lambda) = M_p(\lambda)g_{p,m}(\lambda)Q(\lambda, \sigma), \quad (8)$$

where λ denotes the dependence on photon wavelength (or energy), and the three contributing terms are the HRMA effective area $M_p(\lambda)$ for the relevant *part* (e.g., MEG combines the area of HRMA shells 1 and 3), the effective HETG grating efficiency for the *part*-order $g_{p,m}(\lambda)$, and the ACIS-S quantum detection efficiency $Q(\lambda, \sigma)$. The σ parameter signifies a dependence on the focal-plane spatial location; e.g., at “gap” locations between the individual CCD detector chips, we have $Q(\lambda, \sigma_{\text{gap}}) = 0$. Although not explicitly shown, this ACIS efficiency also depends on other parameters, in particular CCD operating temperature and event grade selection criteria.

The grating effective efficiency $g_{p,m}(\lambda)$ is defined as

$$g_{p=\text{MEG[HEG]},m}(\lambda) = \frac{\sum_{s=1,3[4,6]} M_s(\lambda)g_{s,m}(\lambda)}{\sum_{s=1,3[4,6]} M_s(\lambda)}, \quad (9)$$

where s designates the HRMA shell (the numbering system is a legacy from the original AXAF HRMA design, which had six shells; shells 2 and 5 were deleted to save weight and cost). The grating efficiency values $g_{s,m}(\lambda)$ are the average of the facet efficiency models derived from X-GEF data for all facets on shell s multiplied by a shell vignetting factor (primarily the fraction of the beam not blocked by grating frames; Table 1). The values of these (single-sided) effective efficiencies are plotted for zeroth through third order in Figure 17 for the HEG and MEG grating sets; they are version “N0004,” based on the laboratory measured facet efficiencies and using our updated optical constants.

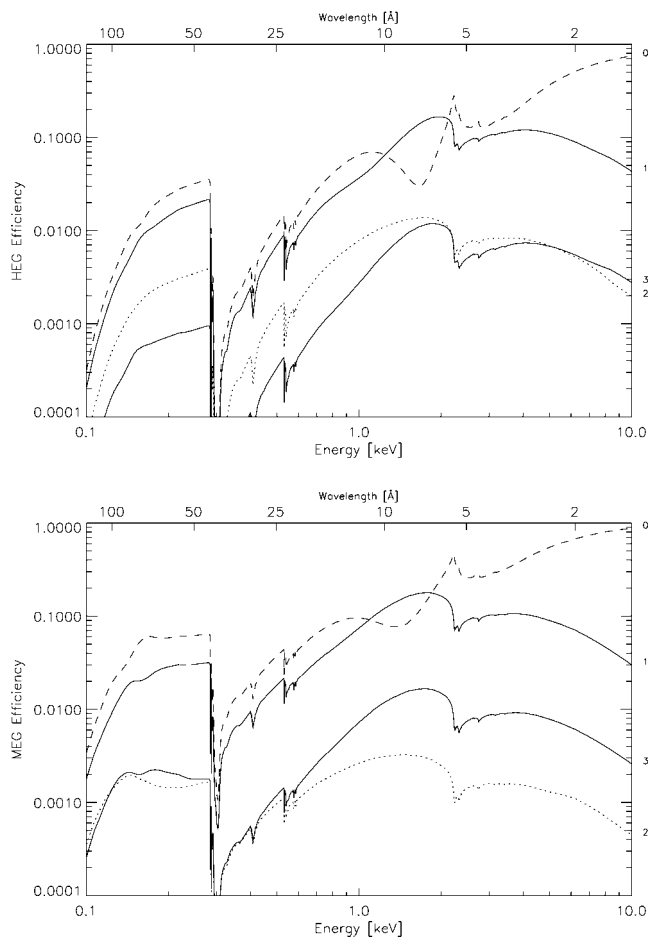


FIG. 17.—HEG and MEG effective diffraction efficiencies. These single-sided efficiencies are the HEG and MEG efficiencies averaged over the sets of facets and weighted by the mirror shell areas. The diffraction order is labeled by the integers to the right of the plots. Note that for the wider-barred HEG, the second order is generally higher than the third order, whereas the MEG shows the more expected suppression of the second order.

4.2.1. Diffraction Efficiency Measurements

In principle, the diffraction efficiency of the HETG can be measured as the ratio of the flux of a monochromatic beam diffracted into an order divided by the flux seen when the HETG is removed from the X-ray beam, a “grating-in over grating-out” measurement. If the same detectors are used in the measurements, then their properties cancel and the efficiency can be measured with few systematic effects. In early testing at XRCF, the HEG and MEG diffraction efficiencies were measured using nonimaging detectors, a flow-proportional counter, and a solid-state detector (Dewey et al. 1997, 1998). The detector’s entrance aperture could be defined by a pinhole of selectable size, typically 0.5 to 10 mm in diameter.

The main complication of these nonimaging measurements results from the complexity of the source spectra and the limited energy resolution of the detectors compared to that of the

HETGS. The Electron Impact Point Source (EIPS) was used to generate K and L lines of various elements, in particular C, O, Fe, Ni, Cu, Mg, Al, Si, Mo, Ag, and Ti. As Figure 14 shows, the “line” typically consists of several closely spaced lines. For the “grating-in” dispersed measurement, only some fraction of these “lines” fall in the pinhole aperture and are detected; e.g., consider the 500 μm aperture indicated in the figure. In contrast, the “grating out” measurement includes all of the lines and any local continuum within the energy resolution element of the low-resolution detector. In order to make a correction for this effect, spectra at HETG resolution, similar to Figure 14, were collected for each X-ray line of interest and used to calculate appropriate correction factors, ranging from a few percent to a factor of 2.

The resulting XRCF efficiency measurements for the HEG and MEG first orders are shown in Figure 18 along with the laboratory-based values (*solid lines*, Fig. 17). In addition to counting statistics, the error bars here include an estimate of the systematic uncertainty introduced in the correction process described. These results confirm the efficiency models derived from X-GEF measurements at the 10%–20% level, but also suggest possible systematic deviations. Because these deviations are small, we waited for flight data before considering any corrections to the efficiency values.

4.2.2. Absolute Effective Area

Absolute effective area measurements were performed at the XRCF with the flight ACIS detector; in particular, the ACIS-S, consisting of a linear array of six CCD detector chips designated S0 through S5 (or CCD_ID = 4–9). Devices at locations S1 and S3 are back-illuminated (BI) CCDs with improved low-energy response. S3 is at the focal point, so it detects zeroth order and is often used without the HETG inserted for imaging observations. S1 is placed to detect the cosmically important lines of ionized oxygen, with enhanced efficiency. Note that there are small gaps between the ACIS-S CCDs, with sizes determined by the actual chip focal plane locations.

The first-order HETGS effective area can be divided into five regions in which different physical mechanisms govern the effective area of the system (variously shown in Figs. 3, 17, 20, and 21):

Below 1 keV.—Absorption by the polyimide membranes of the gratings and the ACIS optical blocking filter and SiO layers limit the effective area and introduce structure, with absorption edges due to C, N, O, and Cr.

1–1.8 keV.—The phase effects of the partially transparent gratings enhance the diffraction efficiency.

1.8–2.5 keV.—Edge structures are seen due to Si (ACIS), Ir (HRMA), and Au (grating).

2.5–5.5 keV.—Effective area is slowly varying, with some low-amplitude Ir (HRMA) and Au (HETG) edge structure. The

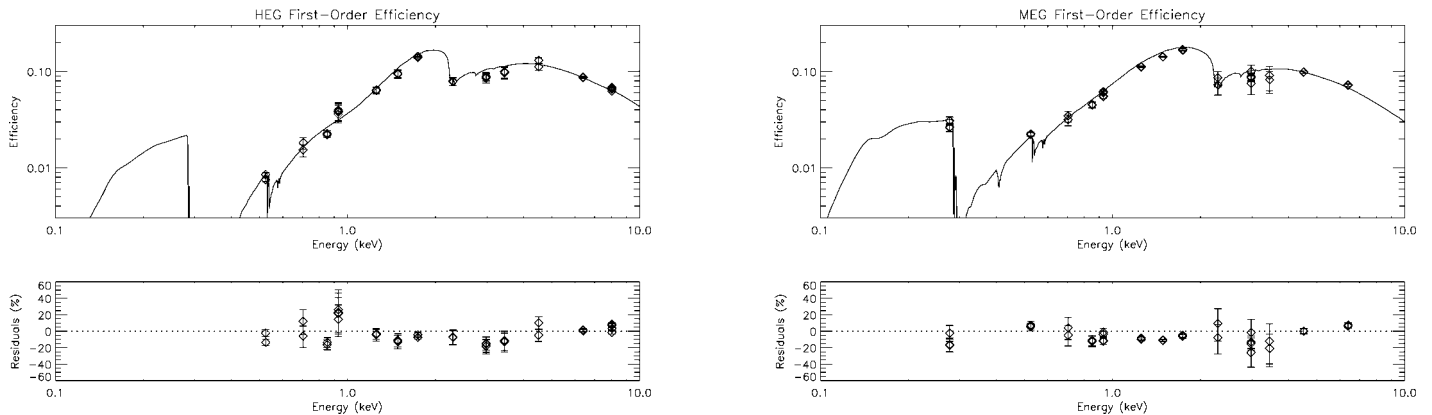


FIG. 18.—HEG and MEG first-order, single-sided diffraction efficiency measurements made with nonflight detectors at XRCF. Error bars include systematic errors that arise from corrections applied due to complex X-ray source line structure and the use of nonimaging detectors; e.g., for the high-energy L lines between 2 and 4 keV. On the whole, the measurements compare well with the expected values (solid line).

efficiency is also phase-enhanced in this region, especially for the HEG.

5.5–10 keV.— The mirror reflectivity, grating efficiency, and ACIS efficiency all decrease with increasing energy, leading to a progressively steepening decline.

The energy range from 0.48 to 8.7 keV was sampled at over 75 energies using X-rays produced by three of the sources of the X-Ray Source System (Kolodziejczak et al. 1995). The DCM provided dense coverage of the range 0.9 to 8.7 keV; the High Resolution Erect Field (grating) Spectrometer (HiREFS) provided data points in the 0.48 to 0.8 keV range; and X-ray lines from several targets of the EIPS covered the range from 0.525 keV (O K) to 1.74 keV (Si K).

The absolute effective area was measured as the ratio of the focal plane rate detected in a line to the line flux at the HRMA entrance aperture. A set of four Beam Normalization Detectors (BNDs) were located around the HRMA and served as the prime source of incident flux determination. The ACIS detector was defocused by 5 to 40 mm to reduce pileup caused when more than one photon arrives in a small region of the detector

during a single integration (Davis 2001b, 2003) by spreading the detected events over a larger detector area, as seen in Figure 19. A variety of analysis techniques and considerations were applied to analyze these data (Schulz et al. 1998). Chief among them for the monochromator data sets were beam uniformity corrections to the effective flux based on extensive measurements and modeling carried out by the MSFC project science group (Swartz et al. 1998). Other corrections were made for line deblending and ACIS pileup. Uncertainties in the measurements were assigned based on counting statistics and estimated systematics; typically, each measurement has an assigned uncertainty of an order of 10%.

Representative results are shown for the MEG $m = -1$ in Figure 20, using ACIS chips S0, S1, S2, and S3, and for the HEG $m = +1$ in Figure 21, detected on chips S3, S4, and S5. Measurements of the HETG combined zeroth order are shown in Figure 22. The data indicate that we are close to realizing our goal of a 10% absolute effective area calibration for the first-order effective area. The measurement-model residuals are seldom outside a $\pm 20\%$ range for both the HEG and MEG

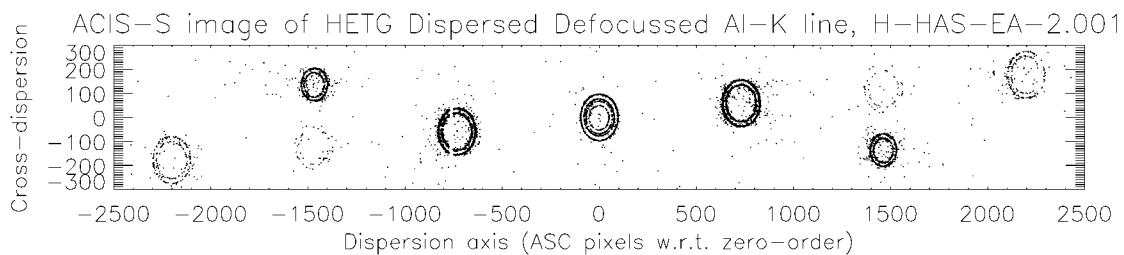


FIG. 19.—ACIS-S defocused image of HETG-dispersed Al K line at XRCF. The rings from the four HRMA shells are visible in the central, zeroth-order image. The HEG and MEG dispersed orders are clearly identified by the corresponding pairs of HRMA shells in their images. Only the $m = \pm 1$ order images are seen for the HEG grating; with less dispersion, the MEG orders $m = \pm 1, \pm 2,$ and ± 3 are all within the image.

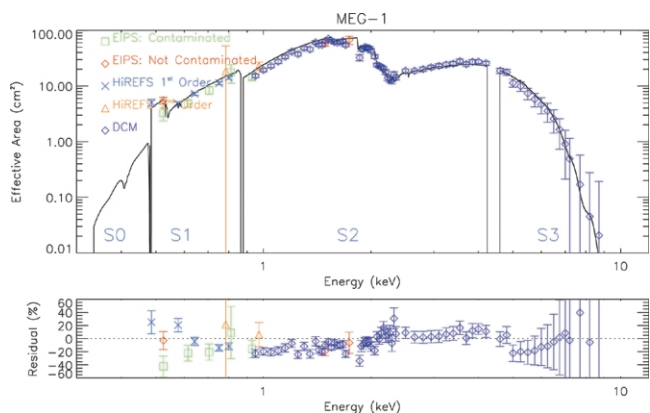


FIG. 20.—Plots of measured and modeled absolute effective area for the HETGS MEG -1 st order with residuals.

first-order areas. Systematic variations of the residuals appear at a level of an order of -20% in the energy range below 1.3 keV; there is agreement better than 10% in the 2.5–5 keV range. The regions of greater systematic variation, 1.3–2.5 keV and above 5 keV, are most likely dominated by uncompensated DCM beam uniformity effects and ACIS pileup effects, respectively.

Effective area measurements for $|m| \geq 2$ were also carried out with the flight focal plane detectors (Flanagan et al. 1998) and show agreement at the 20% level for HEG second and MEG third orders.

4.2.3. Relative Effective Area

In order to probe for small-scale spectral features in the HETGS response, we performed tests at XRCF using a very bright continuum source (Marshall et al. 1998). The EIPS was used with Cu and C anodes and operated at high voltage and low current in order to provide a bright continuum over a wide range of energies. The ACIS-S was operated in a rapid readout mode (“ 1×3 ” continuous clocking mode) to discriminate orders and to provide high throughput.

High-count spectra were created from the data and compared to a smooth continuum model passed through the predicted HETGS effective area (Fig. 23). Many spectral features are observed, including emission lines attributable to the source spectrum. We find that models for the HETGS effective area predict very well the structures seen in the counts spectrum, as well as the observed fine structure near the Au and Ir M edges, where the response is most complex. Edges introduced by the ACIS quantum efficiency (QE) and the transmission of its optical blocking filter are also visible (the Si K and Al K edges, respectively). By comparing the positive and negative dispersion regions, we find no significant efficiency asymmetry attributable to the gratings, and we can further infer that the

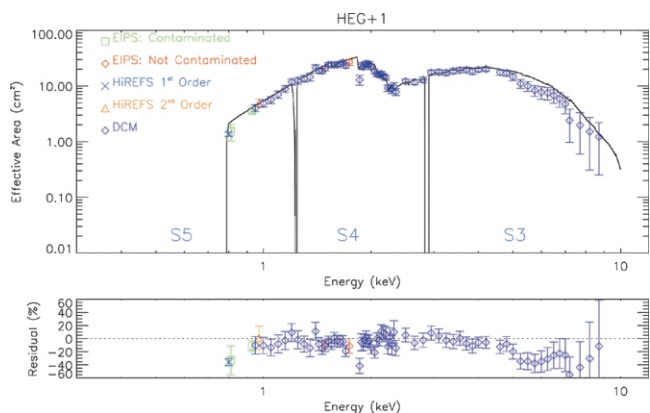


FIG. 21.—Plots of measured and modeled absolute effective area for the HETGS HEG $+1$ st order with residuals.

QEs of all the ACIS-S frontside illuminated (FI) chips are consistent to $\pm 10\%$.

5. FIVE YEARS OF FLIGHT OPERATION

5.1. Flight Data Examples

The first flight data from the HETG were obtained on 1999 August 28 while pointing at the active coronal binary star Capella. Subsequent observations of this and other bright sources provided in-flight verification and calibration. The instrument performance in orbit is very close to that measured and modeled on the ground. A recent summary of *Chandra*'s initial years is given by Weisskopf et al. (2004), and Paerels & Kahn (2003) review some aspects of high-resolution spectroscopy performed with *Chandra* and *XMM-Newton*.

Figure 24 shows 26 ks of data from Capella. The top panel shows an image of detected events on the ACIS-S detector, with the image color indicating the ACIS-determined X-ray

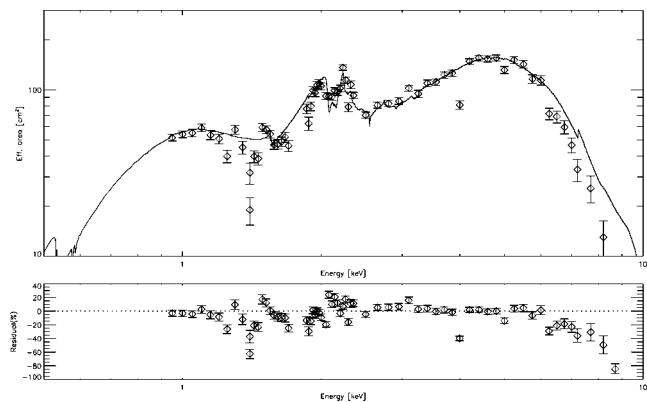


FIG. 22.—Plot of measured and modeled absolute effective area for the HETGS HEG and MEG combined, zeroth order with residuals.

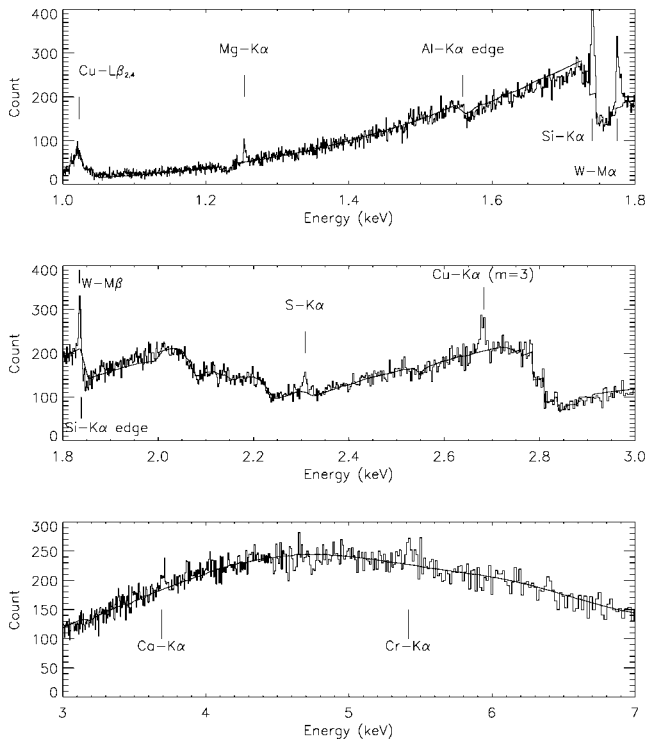


FIG. 23.—HEG spectrum of the Cu continuum source. These plots show an expanded view of the measured spectrum (finely binned histogram) overlaid with a model based on a smooth underlying source spectrum folded through the mirror, grating, and detector responses. The well-modeled detailed structure of the “bumps and wiggles” in the observed counts spectrum indicates an accurate relative effective area calibration. In addition to the expected bright continuum, note the many weaker lines due to contaminants in and on the source target.

energy. In this detector coordinate image, the features are broad due to the nominal observing mode in which the spacecraft pointing is intentionally “dithered” to average over small-scale detector nonuniformities. The ACIS-S chips are numbered S0 to S5 from left to right, with the aim point in S3, where the bright undispersed image is visible and includes a vertical frame-transfer streak. HETG-diffracted photons are visible, forming a shallow X pattern. The middle panel shows an image after the data have been aspect-corrected and data selections applied to include only valid zeroth- and first-order events. The lower set of panels shows an expanded view of the MEG $m = -1$ spectrum, with emission lines clearly visible. The observed lines and instrument throughput are roughly as expected (Canizares et al. 2000).

As a demonstration of the high resolving power of the HEG grating, a close-up of the 9.12 to 9.35 Å spectral region of a Capella observation is shown in Figure 25. The three main lines seen here are from $n = 2$ to 1 transitions of the He-like Mg^{+10} ion, designated “Mg xi”; a resolving power of ≈ 850 is being achieved here, with a FWHM of ≈ 1.6 eV.

5.2. Flight Instrument Issues

Since the HETGS is a composite system of the HRMA, HETG, ACIS, and spacecraft systems, the HETGS flight performance is sensitive to the properties of all of these systems. The various flight issues that have arisen in the past 5 years are summarized here by component, and their effect on the HETGS performance is mentioned. A complete account of these issues is beyond the scope of this paper; further details of the in-flight HETG calibration are presented in Marshall et al. (2004). See also documents and references from the *Chandra* X-ray Center (CXC 2004), which also archives and maintains specific calibration values and files in the *Chandra* Calibration Database (CALDB), along with extensive release notes.

5.2.1. HRMA Issues

The HRMA (van Speybroeck et al. 1997) is the heart of the observatory and has maintained a crisp, stable focus for 5 years; the commanded focus setting has remained the same for 5 years. The HETG resolving power has remained stable as well indicating stability of the grating facets and overall assembly. Details of the HRMA PSF in the wings are still being worked but this has minimal effect on the HETG LRF/RMF in practical application.

The only issue arising in flight related to the HRMA is seen as a slight step increase (15%) in effective area in the region near the Ir M-edge—seen clearly in HETGS spectra. A model based on the reflection effect of a thin contamination layer on the HRMA optical surfaces agrees reasonably with the deviations seen, Figure 26, implying a hydrocarbon layer thickness of 20 ± 5 Å. At present there is no evidence that the layer thickness is changing significantly with time; detailed modeling and updates to the calibration products are in progress.

5.2.2. ACIS Issues

In the first flight data sets, slight wavelength differences were seen between the plus and minus orders, indicating a few pixel error in our knowledge of the relative locations of the ACIS-S CCDs. The ACIS geometry values were adjusted for this in 1999 to an accuracy of ~ 0.5 pixels. As a by-product of our HETG LSF work (see below), these values have been updated a second time to an accuracy of ~ 0.2 pixels, and they show a stability at this level over the first 5 years of flight.

The ACIS pixel size as fabricated was precisely quoted as $24.000 \mu\text{m}$, and this value was used for initial flight data analysis. However, it was later realized that this value was for room temperature—at the flight operating temperatures of an order of -120°C , the pixel size was determined to be $23.987 \mu\text{m}$, and this value has been incorporated into the analysis software, etc.

Order separation is performed using the intrinsic energy resolution of the ACIS CCDs, as demonstrated in Figure 27 for

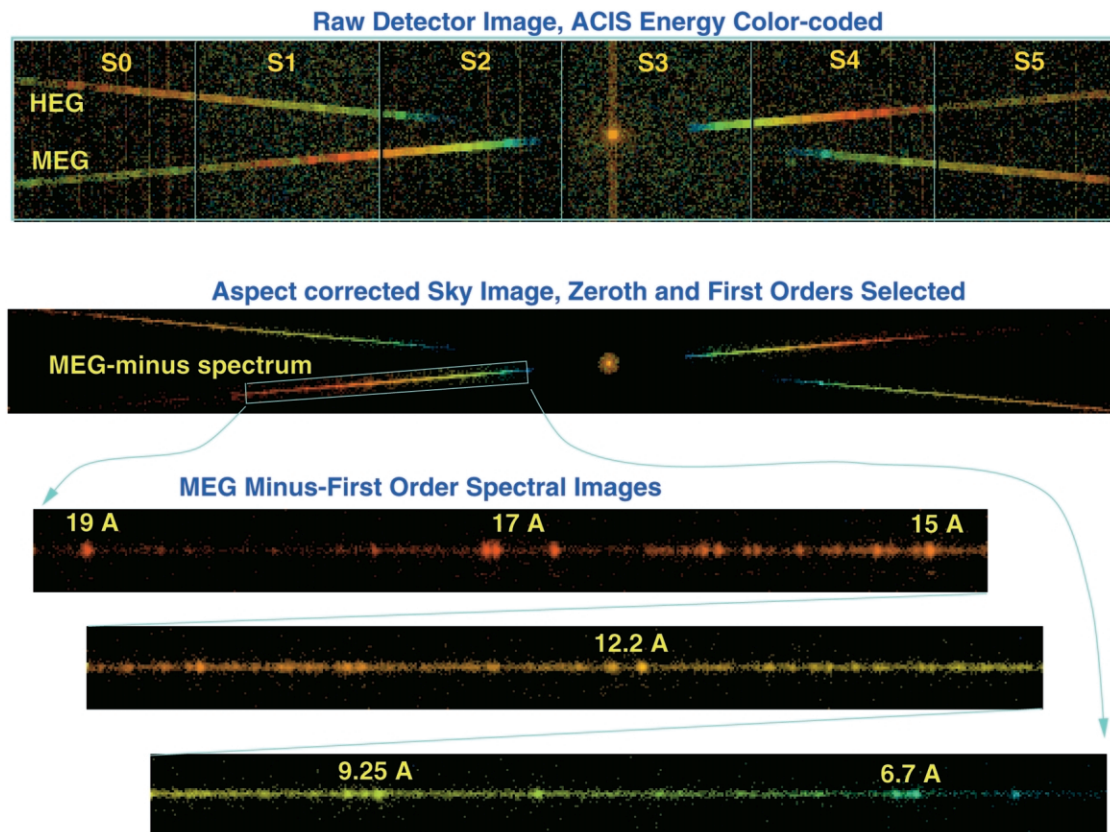


FIG. 24.—Flight HETGS observation of Capella. In the top image, the HETG spreads the HRMA-focused X-rays into a shallow X pattern on the ACIS-S detector, and the spacecraft dither broadens the image. In the middle image, the zeroth-order and dispersed images are sharper because of aspect correction. (Note that this sky-coordinates image has been rotated and flipped to match the detector-image orientation.) At bottom, a wealth of spectral information is seen in the expanded MEG minus first-order spectral image, showing bright emission lines.

a Capella observation. ACIS suffered some radiation damage early in the mission, which degraded the energy resolution of the FI chips (Townsend et al. 2000); relevant to the HETGS are FI chips S0, S2, S4, and S5. However, as seen in the figure, the resolution of those CCDs is still sufficient to permit clean separation of the HETG orders. The CXC pipeline software generally includes 95% of the first-order events in its order selection; the exact fraction depending on CCD and energy is calculated and included in the creation of HETGS ARF response files.

The ACIS detector suffers from pileup (Davis 2001b), and this was expected in the bright zeroth-order image. However, pileup also shows up in the dispersed spectra of bright sources and/or bright lines; algorithms have been developed to ameliorate this pileup (Davis 2003).

Early in the mission, there were indications in LETG-ACIS data that the C K edge of the ACIS optical blocking filter (OBF) was deeper than predicted. Later it was realized that a contaminant was building up on the ACIS OBF, and hence the effective ACIS QE was decreasing (Marshall et al. 2004). The main spectral, temporal, and spatial effects of this contaminant have

now been incorporated into *Chandra* responses; the composition and properties of the contaminant are the focus of continued measurement and modeling.

Comparison of the plus and minus orders of the HETGS lead to a measurement of a discrepancy of the QEs of the ACIS FI CCDs compared to ACIS back-illuminated CCDs (S1 and S3). This issue was recently resolved into two components: the FI devices suffer from cosmic-ray dead-time effects of an order of 4%, and the BI QEs are actually somewhat larger than initially calibrated. The BI QEs were updated in 2004 August (CALDB, ver. 2.28) and are thus now included in HETGS ARFs.

5.2.3. HETG Issues

All the essential parameters for the HETG in flight are the same or consistent with the ground values. Some notable quantities are discussed below.

1. *Clocking Angle*.—The flight angles of the HEG and MEG dispersion axes measured on the ACIS-S are given in Table 1; these values are in agreement with the XRCF-measured values.

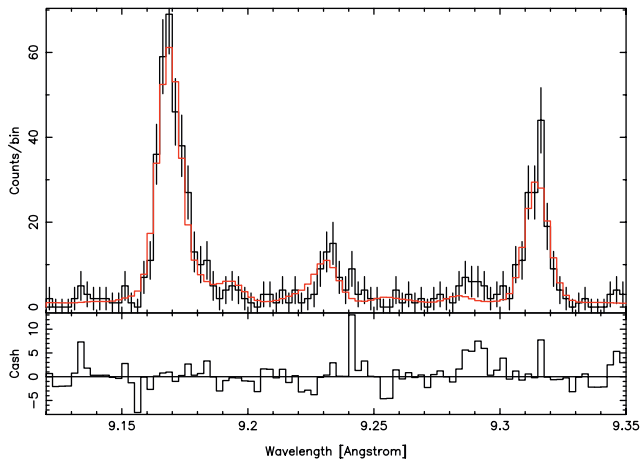


FIG. 25.—Example of HEG resolving power and modeled LRF. Shown is a close-up of the He-like Mg line complex near 9.25 Å (1.34 keV), as seen by the HEG in 40.5 ks of Capella data (histogram). A model folded through the HEG instrumental response is also shown (red) and has a FWHM of the order of 11 mÅ (1.6 eV), for a resolving power of ≈850.

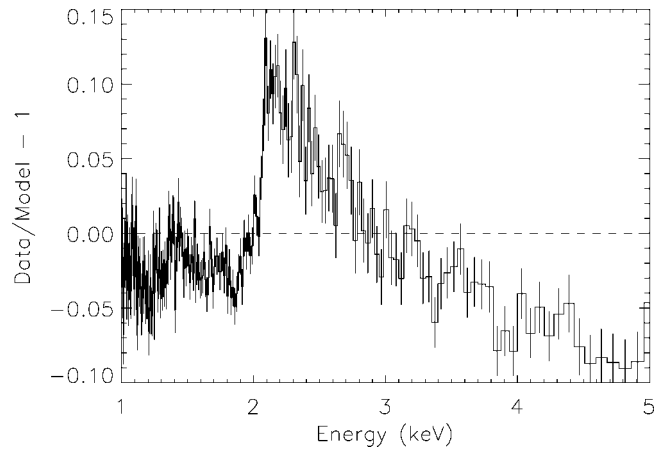


FIG. 26.—Deviations at the Ir edge, seen with HETG. The HETG counts spectrum clearly shows the structure of the residual between data and model at the Ir edge and extending to higher energies. Note that the full range plotted here is only -10% to 15%. This structure can be reasonably explained as the effect of a 20 Å hydrocarbon contaminant layer on the HRMA.

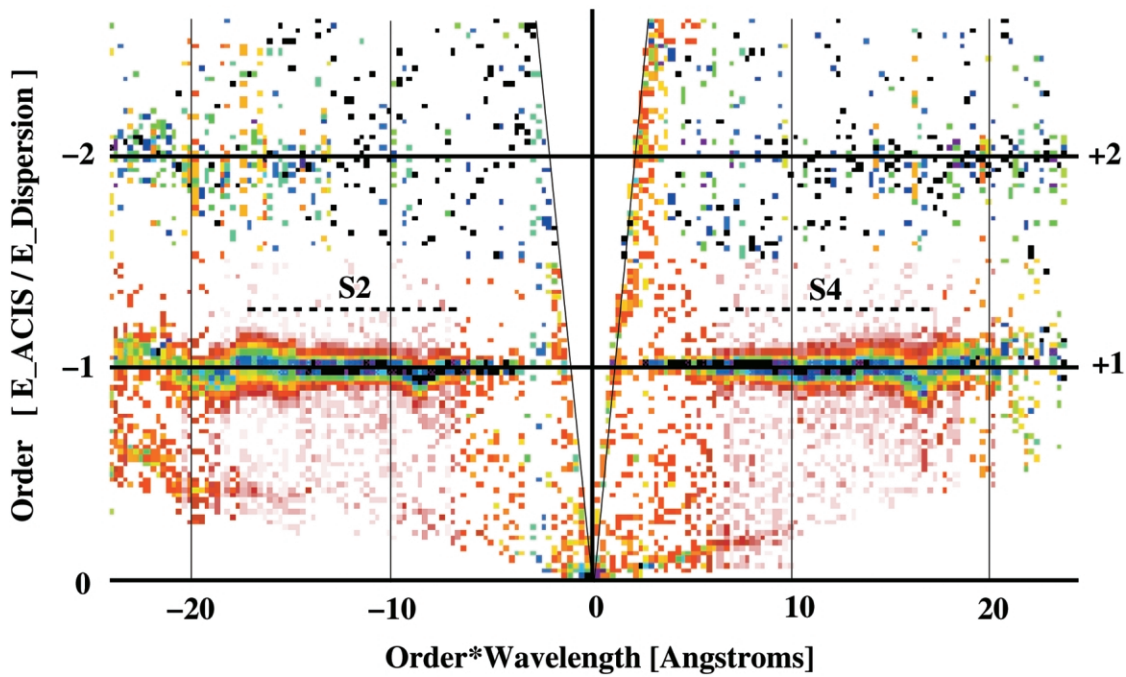


FIG. 27.—Order separation with the ACIS-S. The intensity of MEG events extracted from a Capella observation (ObsID 3674) are indicated by color (from red to blue/black) in order, m , vs. dispersion, $m\lambda$, space. The x -axis is equivalent to the dispersion location of the events, and the y -axis is the CCD-determined energy expressed as the “order”: $m = E_{ACIS}/E_{Dispersion}$. The regions read out by FI CCDs S2 and S4 are indicated; even with their degraded resolution, the order selection can be done with high efficiency.

2. *Rowland Geometry and Spacing.*—An accurate account of the Rowland geometry and spacing is crucial to achieve the best focus of the dispersed spectra on the detector. The Rowland geometry of the HETG was demonstrated during initial plate-focus tests: dispersed line images from a range of wavelengths came to their best dispersion-direction focus at a common detector focus value that agreed with the ACIS-S3 best-imaging focus value within $50\ \mu\text{m}$. The spacing of the HETG from the focal plane (the Rowland spacing) appeared initially to be off from the expected value until the ACIS pixel size change with temperature was included (§ 5.2.2). Currently, the HETG Rowland spacing in flight (given in Table 1) is the value produced by ground installation metrology.

3. *Grating Period.*—The accuracy of the HETG-measured wavelength depends strongly on the assigned grating period. For the first years of use, the grating periods of the HEG and MEG were set to the laboratory measurement results. However, recent analysis of Capella data over 5 years shows the MEG-derived line centroid to be off by $40.2 \pm 5\ \text{km s}^{-1}$ compared to the (apparently accurate) HEG values (see Fig. 28). Hence, the MEG period has recently (CALDB ver. 3.0.1, 2005 February) been set to $4001.95\ \text{\AA}$, which makes the MEG/HEG line centroids mutually consistent. Note that the stability of the wavelength scale is good to $10\ \text{km s}^{-1}$, or 30 ppm over 5 years.

4. *Dispersion and Cross-Dispersion Profiles.*—Recently, the HETG LRFs have been modeled as a linear combination of two Gaussians and two Lorentzians to encode improved fidelity with the latest results of MARX ray-trace models (Marshall et al. 2004); these LRF products are available in *Chandra* CALDB versions 2.27 and higher. A Capella in-flight calibration data set (ObsID 1103) has been used to verify the quality of the LRFs. Using a multitemperature APED thermal model (Brickhouse 1996), the He-like line complex of Mg xi has been fitted with the grating line response functions. Thermal broadening of Mg xi species has been taken into account in order to measure its line width properly. Figure 25 shows the result of this model fitting. The derived line widths are essentially in agreement with having no excess broadening, as expected for static coronal emission. Note that the wings of the grating line response functions (2 orders of magnitude below the peak when a few FWHMs away) are generally well below the actual continuum and pseudo-continuum levels in celestial sources, and so flight-dispersed data do not help calibrate the wings of the LRF in general.

In the cross-dispersion direction, we parameterize the fraction of energy “encircled” in an arbitrary rectangular region (the encircled energy fraction, or EEF) and include this in the analysis software. The calibration values encoded into LRFs are generally consistent with observations. An uncertainty of 1%–3% may be introduced by the EEF term, although other quantitative uncertainties (e.g., HRMA effective area) are comparable or greater at this point in HETGS calibration.

5. *HETG Efficiency Calibration.*—After 5 years of flight operation, the efficiencies of Figure 17, based on the facet

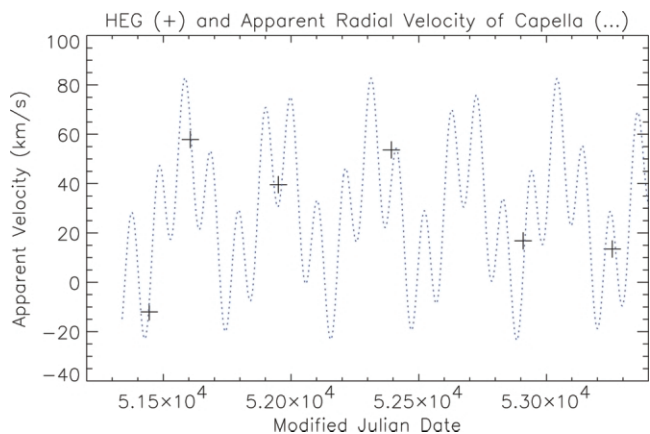


FIG. 28.—Stability of the HETG wavelength scale over 5 years. The measured line centroid variation from Capella observations (+) shows agreement and stability with the predicted Capella Doppler motion at the $10\ \text{km s}^{-1}$ level.

laboratory measurements, have not been adjusted and are still used to create ARFs for flight observations. Likewise, no additional features or edges have been ascribed to the HETG instrument response beyond what is in these calibration files. Comparing HEG and MEG spectra of bright continuum sources, there are data to support making a *relative* correction of the HEG and MEG efficiencies to bring their measured fluxes into agreement. This relative efficiency correction is small, in the range 0% to -7% if applied to the MEG, and varies smoothly in the $2\text{--}15\ \text{\AA}$ range. This final “dotting the i” of HETG calibration is nearing completion and will be included in upcoming CXC calibration files.

5.3. Discussion

As the minimal effect on the HETGS performance of the various flight issues described above indicates, the HETGS has and is performing essentially as designed, yielding high-resolution spectra of a broad range of astrophysical sources. Some calibration issues are still being addressed, but these are at the $\sim 10\%$ level in the ARF and the fractions-of-a-pixel level in the grating LRF/RMF.

It is useful to put the *Chandra* gratings performance in perspective with each other and with the Reflection Grating Spectrometer (RGS) on *XMM-Newton*. The effective areas for these grating instruments are shown in Figure 29; note the complementary nature of the instruments in various wavelength ranges. The advance in resolving power these dispersive instruments have provided is clearly seen in Figure 30, compared to the ACIS CCD resolving power values shown there as well. A line for the resolving power of a 6 eV FWHM microcalorimeter (e.g., *Astro-E2*; now *Suzaku*) is plotted, and also shows the uniqueness of the grating instruments in the range below 2 keV.

The high resolution and broad bandpass of the HETGS have

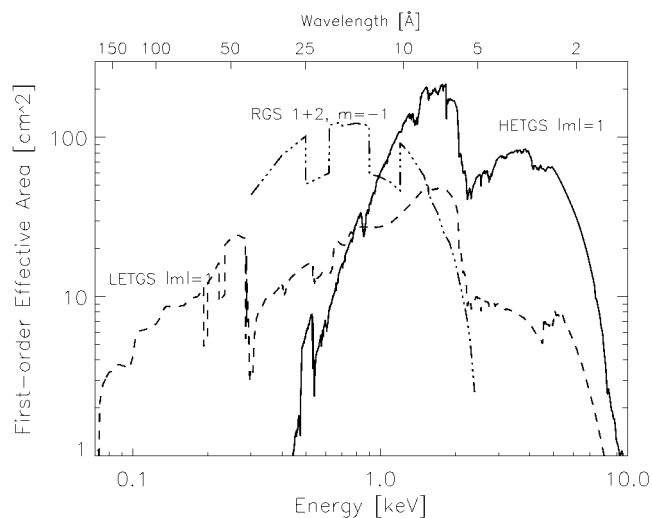


Fig. 29.—Effective areas for the *Chandra* HETGS (HEG+MEG) and LETG gratings and the Reflection Grating Spectrometers (RGS 1+2) on *XMM-Newton*. The combined first-order areas are plotted for each instrument.

made it the instrument of choice for many observers. In the first 5 years of *Chandra* operation, the HETGS was used in over 400 observations totaling approximately 20 Ms of exposure time. This represents about 17% of *Chandra*'s total observation time for that period. As is typical of spectroscopy at other wavelengths, HETGS observations tend to be long, ranging from tens of ks for bright Galactic sources to hundreds of ks for active galactic nuclei (AGNs). A review of the results of these observations is outside the scope of this paper; some examples can be found in Weisskopf et al. (2002, 2004) and Paerels & Kahn (2003).

The HETG is the product of nearly two decades of research and development in the MIT Center for Space Research, now the MIT Kavli Institute (MKI) to adapt the techniques of micro- and nano-structure fabrication developed primarily for microelectronics to the needs of X-ray astronomy. The initial concept emerged from nanostructure research conducted by one of us (H. I. S. and collaborators) in the MIT Nano Structures Laboratory of the Research Laboratory of Electronics (and previously at MIT Lincoln Laboratory). We thank Al Levine, Pete Tappan, and Bill Mayer for initial HETG design evaluations.

The Space Nanotechnology Laboratory was established in MKI under the leadership of HETG Fabrication Scientist M. L. S. to advance the technology and then execute the fabrication of the flight hardware. Significant processing support was provided by the MIT Microsystems Technology Laboratory. Fabrication engineering support was provided by Rich Aucoin, Bob Fleming, Pat Hindle, and Dave Breslau. Facet

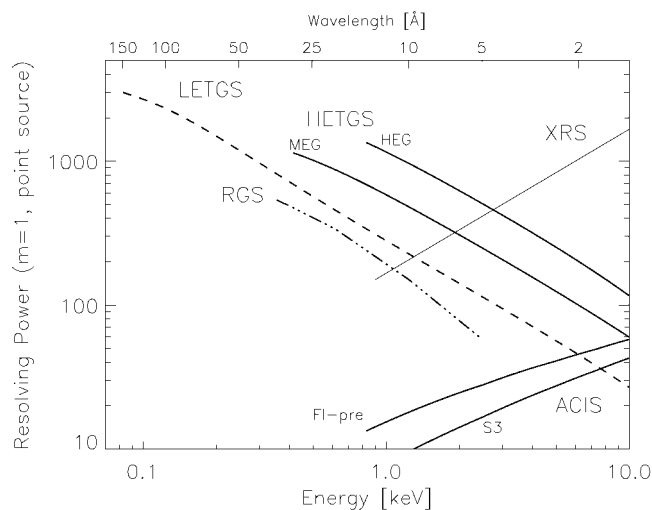


Fig. 30.—Resolving power in first order for the *Chandra* gratings, HEG, MEG, and LETG, and the RGS on *XMM-Newton*. For reference, representative resolving powers of the nondispersive *Chandra* ACIS FI (prelaunch) and BI (S3) detectors and a microcalorimeter X-ray Spectrometer (XRS; FWHM = 6 eV) are shown as well.

fabrication was carried out by Jeanne Porter, Bob Sission, Roger Millen, and Jane Prentiss.

D. D. (Instrument Scientist), M. M. (Systems Engineer), and K. A. F. led the overall design and ground calibration activities. J. E. D. provided efficiency modeling algorithms and software. Design and test engineering support was provided by Chris Pak, Len Bordzol, Richard Elder, Don Humphries, and Ed Warren. Facet testing was carried out by Mike Enright and Bob Laliberte, who assembled the flight HETG.

H. L. M. carried out much of the XRCF test planning and analyses. M. W. and D. P. H. provided modeling and analysis support. N. S. S. analyzed key XRCF data, as did Sara Ann Taylor and Michael Stage. Many of the authors were involved in flight calibration; K. I. carried out detailed flight LSF work. Finally, focus and progress were maintained under the overall leadership of C. R. C. (Instrument Principal Investigator), supported by T. L. M. as Project Scientist through much of the design and development phase, and E. B. G. as Project Manager (Galton 2003).

The HETG team acknowledges conspicuous and inconspicuous support from our colleagues at the MKI and from the many groups involved in the *Chandra* project, specifically MSFC Project Science, Smithsonian Astrophysical Observatory, TRW, and Eastman Kodak. We thank John Kramar and colleagues at NIST for LR period calibration.

Finally, we thank our fellow citizens: this work was supported by the National Aeronautics and Space Administration, under contracts NAS8-38249 and NAS8-01129 through the Marshall Space Flight Center.

APPENDIX A

MULTIVERTEX EFFICIENCY EQUATIONS

Assuming the validity of scalar diffraction theory and ignoring reflection and refraction, the m th-order grating efficiency for a perfect diffraction grating is $|F_m(k)|^2$, where the structure factor $F_m(k)$ is given by

$$F_m(k) = \frac{1}{p} \int_0^p dx e^{i2\pi mx/p + i\phi(k, x)}, \quad (\text{A1})$$

where p is the grating period, $k = 2\pi/\lambda$ is the wavenumber, and $\phi(k, x)$ is a phase shift introduced by the grating bars. The phase shift is a function of energy or wavenumber k and also depends on the grating bar shape, according to

$$\phi(k, x) = -k[\delta(k) - i\beta(k)]z(x), \quad (\text{A2})$$

where δ and β are energy-dependent functions related to the dielectric constant of the grating bars. The function $z(x)$ represents the path length of the photon as it passes through a grating bar; it is sometimes called (rather loosely) the “grating bar shape,” and more rigorously, the “path-length function.”

It is preferable to work with the unitless quantity $\xi = x/p$ and to parameterize the path-length function in terms of it. For simplicity, we represent $z(\xi)$ as a piecewise sum of N line segments; i.e.,

$$z(\xi) = \sum_{j=0}^{N-1} (a_j + b_j \xi) B(\xi_j \leq \xi \leq \xi_{j+1}), \quad (\text{A3})$$

where $B(X)$ is the boxcar function defined to be 1 if X is true, or zero otherwise. By demanding that the path-length function be continuous, it is easy to see that the coefficients a_j and b_j

are given by

$$a_j = \frac{z_j \xi_{j+1} - z_{j+1} \xi_j}{\xi_{j+1} - \xi_j}, \quad (\text{A4})$$

$$b_j = \frac{z_{j+1} - z_j}{\xi_{j+1} - \xi_j}, \quad (\text{A5})$$

where $z_j = z(\xi_j)$. For obvious reasons, we require $z_j \geq 0$ and that the set of points $\{\xi_j\}$ be ordered according to

$$0 = \xi_0 \leq \xi_1 \leq \dots \leq \xi_{N-1} \leq \xi_N = 1. \quad (\text{A6})$$

The most redeeming feature of this particular parameterization of the path-length function is that the integral appearing in equation (A1) may be readily evaluated with the result

$$F_m(k) = i \sum_{j=0}^{N-1} e^{-ika_j} \frac{e^{-i\xi_{j+1}(\kappa b_j + 2\pi m)} - e^{-i\xi_j(\kappa b_j + 2\pi m)}}{\kappa b_j + 2\pi m}, \quad (\text{A7})$$

where

$$\kappa = k[\delta(k) - i\beta(k)] \quad (\text{A8})$$

is complex. Although one can carry out the algebraic evaluation of $|F_m(k)|^2$ using the above expression, it is very tedious, and the result is not particularly illuminating. Moreover, it is computationally more efficient to evaluate the above sums numerically using complex arithmetic and then compute $|F_m(k)|^2$ by multiplying by the complex conjugate.

APPENDIX B

ERROR BUDGET FOR FACETED-ROWLAND DESIGN

The response of the HETGS can be crudely yet usefully characterized by the location and FWHM of the LRF core in both the dispersion and cross-dispersion directions. The “resolving power” of the spectrometer is given by $E/dE = y'/dy'$, where y' is the diffraction distance and dy' is the FWHM of the resulting image projected along the dispersion axis. The design of the HETG involved the use of an error budget to assess and root sum square (rss) the various contributions to the dy' term of the resolving power and the corresponding

dz' term in the cross-dispersion. This error budget was useful for studying the dependence of the resolving power on the variation of individual error terms. The error budget results were verified by performing simplified ray traces of single and multiple facets.

The error budget presented in Table 2 includes all of the important error terms for the flight HETGS resolving power and cross-dispersion blur. Note that the finite facet error term (eq. [5]) is *not* included here, because it is quite small for the

TABLE 2
SIMPLIFIED RESOLVING POWER ERROR BUDGET

Error Description	Symbol	Value	Dispersion Blur	Cross-Dispersion Blur
Blur sources	$\sigma_{y,i}$	$\sigma_{z,i}$
Optics PSF (arcsec rms diameter)	D_{PSF}	≈ 0.6	eq. (B1) or (B2) [(B3)]	eq. (B1) or (B2) [(B3)]
Aspect (arcsec rms diameter)	a	≈ 0.34	eq. (B4)	eq. (B4)
Detector pixel (mm)	L_{pix}	0.023987	eq. (B5)	eq. (B5)
Dither rate (arcsec/frame time)	R_{dither}	0.16	eq. (B6)	eq. (B6)
Defocus with astigmatism (mm)	dx	0.1	eq. (B7)	eq. (B8)
Period variation	dp/p	235 (146)
Roll variation (arcmin rms)	γ	1.8	...	eq. (B10)
Total blur	$\sigma_y^{\text{tot}} = \sqrt{\sum_i \sigma_{y,i}^2}$	$\sigma_z^{\text{tot}} = \sqrt{\sum_i \sigma_{z,i}^2}$
Resolving power	$E/dE = \beta X_{\text{RS}} / (2.35 \sigma_y^{\text{tot}})$...
Input Parameters:				
Energy (keV)	E	As desired
Period (Å)	p	4001.95 (2000.81)
Effective radius (mm)	R_0	470.0 (330.0)
Rowland spacing (mm)	X_{RS}	8632.65
Focal length (mm)	F	10070.0
Derived Values:				
Wavelength (Å)	λ	12.3985/E
Diffr. angle (rad)	β	$\arcsin(m\lambda/p)$
Rowland offset (mm)	$\Delta X_{\text{Rowland}}$	$\beta^2 X_{\text{RS}}$

NOTES.—The major parameters and terms that contribute to the HETGS LRF blur are listed here in a spreadsheet-like format. The effective rms contributions to the dispersion and cross-dispersion blur are given by the referenced equations in Appendix B. As shown, these blurs are rss'ed together, giving the size of the Gaussian LRF core in each direction, σ_y^{tot} and σ_z^{tot} . The resolving power, E/dE , is also calculated as indicated. Current flight parameter values are given here; entries that differ for the MEG and HEG gratings are shown as “MEG value (HEG value).”

HETG design. For compactness, the error equations are referenced in the table and given, with discussion, in the following text.

1. *Optics PSF blur.*—If the optic produces a roughly symmetric Gaussian-like PSF with an rms diameter of D_{PSF} arcseconds, then the Gaussian σ of the one-dimensional projection of the PSF is given, in units of mm in the focal plane, by

$$\sigma_y = \sigma_z = \sigma_H = \frac{1}{2} \frac{\sqrt{2}}{2} F D_{\text{PSF}} \left(\frac{1}{57.3} \right) \left(\frac{1}{3600} \right), \quad (\text{B1})$$

where F is the focal length of the optic (Table 2). This equation is useful when specific models of the optic PSF are not available.

The above equation for σ_H can be extended in two respects, given knowledge of the optic. First, there is generally a dependence on energy that is slowly varying; thus, σ_H can be expressed as, say, a polynomial in $\log_{10} E$. Second, in the case of *Chandra*, the PSF of the mirror shells is more cusplike than Gaussian. This cusplike PSF causes the *effective* σ of the PSF projection to depend on the scale at which it is used; that is, the size of other error terms it is convolved with. The following equations give good approximations to the value of σ_H for HETGS purposes. Blurs for the HEG and MEG mirror sets are

given separately:

$$\begin{aligned} \sigma_{H, \text{MEG}} = & 0.00998 + 0.00014 \log_{10} E + \\ & -0.00399 \log_{10}^2 E + 0.000505 \log_{10}^3 E \end{aligned} \quad (\text{B2})$$

$$\begin{aligned} \sigma_{H, \text{HEG}} = & 0.01134 + 0.00675 \log_{10} E + \\ & -0.01426 \log_{10}^2 E + 0.01133 \log_{10}^3 E \end{aligned} \quad (\text{B3})$$

2. *Aspect blur.*—Aspect reconstruction adds a blur that is expected to be of an order of $a = 0''.34$ rms diameter for *Chandra*. The resulting one-dimensional rms σ is thus

$$\sigma_y, \sigma_z = \frac{1}{2} \frac{\sqrt{2}}{2} F a \left(\frac{1}{57.3} \right) \left(\frac{1}{3600} \right), \quad (\text{B4})$$

where F is the HRMA focal length in mm.

3. *Detector pixel-size blur.*—This error term is the spatial error introduced by the detector readout scheme. For a pixelated detector like ACIS, we assume that the PSF drifts with respect to the detector pixels and that there is a uniform distribution of the centroid location in pixel phase. In this case, the reported

location of an event is the center of the pixel, when in fact the event may have actually arrived ± 0.5 pixel from the center. The rms value of such a uniform distribution is 0.29 times the pixel size:

$$\sigma_y = \sigma_z = 0.29L_{\text{pix}}. \quad (\text{B5})$$

If a uniform randomization of the pixel value is applied during analysis, then a further uniform blur is added in quadrature, adding a factor of $\sqrt{2}$.

4. *Dither rate blur*.—A blur is added because the arrival time of a photon at the ACIS detector is quantized in units of a frame time. The parameter R_{dither} is the maximum dither rate expressed in units of arcseconds per frame time and results in a blur term of

$$\sigma_y, \sigma_z = 0.29 \frac{\sqrt{2}}{2} FR_{\text{dither}} \left(\frac{1}{57.3} \right) \left(\frac{1}{3600} \right), \quad (\text{B6})$$

where the factor of $\sqrt{2}/2$ is present because the dither pattern is sinusoidal.

5. *Defocus and astigmatism blurs*.—Including the effect of a defocus dx and a factor converting the peak-to-peak blur into an rms equivalent, we get the following equations for the Rowland astigmatism contribution to the error budget in dispersion and cross-dispersion directions:

$$\sigma_y = 0.354 \frac{2R_0}{X_{\text{RS}}} dx, \quad (\text{B7})$$

$$\sigma_z = 0.354 \frac{2R_0}{X_{\text{RS}}} (\Delta X_{\text{Rowland}} + dx). \quad (\text{B8})$$

These equations assume that the detector conforms to the Rowland circle, except for an overall translation by dx (positive toward the HRMA). The values of R_0 used in the error budget are effective values—weighted combinations of the relevant mirror shells.

5. *Grating period and roll Variation blurs*.—There are two main error terms that depend on how well the HETG is built: (1) period variations within and between facets (“ dp/p ”), and (2) alignment (“roll”) variations about the normal to the facet surface within and between facets. The period variations lead to an additional blur in the dispersion direction:

$$\sigma_y \approx \beta X_{\text{RS}} \frac{dp}{p}, \quad (\text{B9})$$

where dp/p is the rms period variation. The roll errors lead to additional blur in the cross-dispersion direction through the equation

$$\sigma_z \approx \beta X_{\text{RS}} \gamma \left(\frac{1}{57.3} \right) \left(\frac{1}{60} \right), \quad (\text{B10})$$

where γ is the rms roll variation in units of arcminutes.

REFERENCES

- Agarwal, B. K. 1991, *X-Ray Spectroscopy* (2nd ed.; Berlin: Springer)
- Anderson, E. H., Levine, A. M., & Schattenburg, M. L. 1988, *Appl. Opt.*, 27, 3522
- Beuermann, K. P., Bräuniger, H., & Trümper, J. 1978, *Appl. Opt.*, 17, 2304
- Blake, R. L., et al. 1993, *Proc. SPIE*, 1742, 219
- Born, M., & Wolf, E. 1980, *Principles of Optics* (6th ed; New York: Pergamon)
- Brickhouse, N. S. 1996, in *IAU Colloq. 152, Astrophysics in the Extreme Ultraviolet*, ed. S. C. Bowyer & R. F. Malina (Dordrecht: Kluwer), 105
- Brinkman, A. C., et al. 2000, *ApJ*, 530, L111
- Canizares, C. R., Schattenburg, M. L., & Smith, H. I. 1985, *Proc. SPIE*, 597, 253
- Canizares, C. R., et al. 1987, *ApJ*, 26, L87
- . 2000, *ApJ*, 539, L41
- Chandra X-Ray Center. 2004, *Chandra X-ray Center 2004, Proposers' Observatory Guide*, ver. 7 (Cambridge: CXC), <http://cxc.harvard.edu/proposer/POG>
- Davis, J. E. 2001a, *ApJ*, 548, 1010
- . 2001b, *ApJ*, 562, 575
- Davis, J. E. 2003, *Proc. SPIE*, 4851, 101
- Davis, J. E., Marshall, H. L., Schattenburg, M. L., & Dewey, D. 1998, *Proc. SPIE*, 3444, 76
- Dewey, D., Drake, J. J., Edgar, R. J., Michaud, K., & Ratzlaff, P. 1998, *Proc. SPIE*, 3444, 48
- Dewey, D., Humpheries, D. N., McLean, G. Y., & Moschella, D. A. 1994, *Proc. SPIE*, 2280, 257
- Dewey, D., et al. 1997, *Proc. SPIE*, 3113, 144
- Fischbach, K. F., et al. 1988, *Proc. SPIE*, 982, 273
- Flanagan, K. A., Dewey, D., & Bordzol, L. 1995, *Proc. SPIE*, 2518, 438
- Flanagan, K. A., Schulz, N. S., Murray, S. S., Hartner, G. D., & Predehl, P. 1998, *Proc. SPIE*, 3444, 106
- Flanagan, K. A., et al. 1996, *Proc. SPIE*, 2808, 650
- . 2000, *Proc. SPIE*, 4140, 559
- Franke, A. E., Schattenburg, M. L., Gullikson, E. M., Cottam, J., Kahn, S. M., & Rasmussen, A. 1997, *J. Vac. Sci. Technol. B*, 15, 2940
- Galton, E. B. 2003, <http://space.mit.edu/HETG/GaltonsGuide.html>
- Garmire, G. P. 1999, *BAAS*, 31, 1515

- Graessle, D., Clark, A. M., Fitch, J. J., Harris, B., Schwartz, D. A., & Blake, R. L. 1996, *Proc. SPIE*, 2805, 18
- Henke, B. L., Gullikson, E. M., & Davis, J. C. 1993, *Atomic Data and Nucl. Data Tables*, 54, 181
- Hettrick, M. C., et al. 2004, *Appl. Opt.*, 43, 3772
- Houck, J. C., & DeNicola, L. A. 2000, in *ASP Conf. Ser.* 216, *Astr. Data Anal. Software and Systems IX*, ed. N. Manset, C. Veillet, & D. Crabtree. (San Francisco: ASP), 591
- Kolodziejczak, J. J., et al. 1995, *Proc. SPIE*, 2515, 420
- Markert, T. H. 1990, in *High-Resolution X-Ray Spectroscopy of Cosmic Plasmas*, ed. P. Gorenstein & M. Zombeck (Cambridge: IAU), 339
- Markert, T. H., Canizares, C. R., Dewey, D., McGuirk, M., Pak, C., & Schattenburg, M. L. 1994, *Proc. SPIE*, 2280, 168
- Markert, T. H., et al. 1995, *Proc. SPIE*, 2518, 424
- Marshall, H. L., Dewey, D., & Ishibashi, K. 2004, *Proc. SPIE*, 5165, 457
- Marshall, H. L., Dewey, D., Schulz, N. S., & Flanagan, K. A. 1998, *Proc. SPIE*, 3444, 64
- Marshall, H. L., Tennant, A., Grant, C. E., Hitchcock, A. P., O'Dell, S. L., & Plucinsky, P. P. 2004, *Proc. SPIE*, 5165, 497
- Marshall, H. L., et al. 1997, *Proc. SPIE*, 3113, 160
- Michette, A. G., & Buckley, C. J. 1993, in *X-Ray Science and Technology* (London: Inst. Phys.), 320
- Murray, S. S., et al. 1998, *Proc. SPIE*, 3356, 974
- Nelson, C. S., et al. 1994, *Proc. SPIE*, 2280, 191
- O'Dell, S. L., & Weisskopf, M. C. 1998, *Proc. SPIE*, 3444, 2
- Paerels, F. B. S., & Kahn, S. M. 2003, *ARA&A*, 41, 291
- Pak, C., & McGuirk, M. 1994, paper presented at AIAA Space Programs and Technologies Conference (paper 94-4566)
- Savas, T., Schattenburg, M. L., Carter, J. M., & Smith, H. I. 1996, *J. Vac. Sci. Technol. B*, 14, 4167
- Schattenburg, M. L. 1984, Ph.D. thesis, Mass. Inst. Tech.
- . 2001, *J. Vac. Sci. Technol. B*, 19, 2319
- Schattenburg, M. L., Aucoin, R. J., & Fleming, R. C. 1995, *J. Vac. Sci. Technol. B*, 13, 3007
- Schattenburg, M. L., Aucoin, R. J., Fleming, R. C., Plotnik, I., Porter, J., & Smith, H. I., 1994, *Proc. SPIE*, 2280, 181
- Schattenburg, M. L., Fuentes, R. I., Czernienko, G., Fleming, R. C., & Porter, J. 1995, *Proc. Mat. Res. Soc.*, 356, 615
- Schattenburg, M. L., et al. 1991, *Opt. Eng.*, 30, 1590
- Schnopper, H. W., et al. 1977, *Appl. Opt.*, 16, 1088
- Schroeder, D. J. 1987, *Astronomical Optics* (Academic Press: San Diego), Chap.14
- Schulz, N. S., Dewey, D., & Marshall, H. L. 1998, *Proc. SPIE*, 3444, 160
- Stage, M. D., & Dewey, D. 1998, *Proc. SPIE*, 3444, 36
- Swartz, D. A., et al. 1998, *Proc. SPIE*, 3444, 189
- Townsley, L. K., Broos, P. S., Garmire, G. P., & Nousek, J. A. 2000, *ApJ*, 534, L139
- van Beek, J., Fleming, R. C., Hindle, P. S., Prentiss, J. D., Ritzau, S., & Schattenburg, M. L. 1998, *J. Vac. Sci. Technol. B*, 16, 3911
- van Speybroeck, L. P., et al. 1997, *Proc. SPIE*, 3113, 89
- Weisskopf, M. C., Brinkman, B., Canizares, C., Garmire, G., Murray, S., & van Speybroeck, L. P. 2002, *PASP*, 114, 1
- Weisskopf, M. C., & O'Dell, S. L. 1997, *Proc. SPIE*, 3113, 2
- Weisskopf, M. C., Tananbaum, H. D., van Speybroeck, L. P., & O'Dell, S. L. 2000, *Proc. SPIE*, 4012, 2
- Weisskopf, M. C., et al. 2004, *Exp. Astron.*, 16, 1
- Wise, M. W., Davis, J. E., Huenemoerder, D. P., Houck, J. C., & Dewey, D. 2000, *MARX 3.0 Technical Manual* (Boston: MIT CSR), <http://space.mit.edu/CXC/MARX>